

Simulating surface soil moisture on sandy beaches

Caroline Hallin^{a,b,*}, Christa van IJzendoorn^a, Jan-Markus Homberger^c, Sierd de Vries^a

^a Faculty of Civil Engineering and Geosciences, Delft University of Technology, Stevinweg 1, 2628 CN, Delft, the Netherlands

^b Faculty of Engineering, Lund University, John Ericssonsv 1, 221 00, Lund, Sweden

^c Department of Environmental Sciences, Wageningen University and Research, Droevendaalsesteeg 2, 6708 PB, Wageningen, the Netherlands

ARTICLE INFO

Keywords:

Soil moisture
Aeolian transport
Beach groundwater
Soil water retention

ABSTRACT

A model that simulates surface moisture content on sandy beaches for aeolian transport applications is developed and integrated into the aeolian transport model AeoliS. The moisture content of a thin surface layer (≈ 2 mm thickness) is computed as a function of wave runup, precipitation, evaporation, percolation, and capillary rise from the groundwater table. The groundwater table is simulated using a modified Boussinesq equation accounting for the overheight due to wave runup. The surface moisture due to capillary rise is simulated with an experimentally determined soil water retention (SWR) curve of the “van Genuchten” type. Hysteresis is accounted for by differentiating between SWR curves for drying and wetting conditions. The model is tested against a data set of 221 point observations of surface moisture from Noordwijk beach in the Netherlands. The measured surface moisture within the study area displays large spatial and temporal variability. The model results display an expected cross-shore gradient of moisture content, but also a large scatter when compared to the data. The scatter may partly be explained by local variability of hydraulic properties that are not accounted for within the model. Despite the scatter, the proposed surface moisture model is a starting point to integrate the transport limiting effect of surface moisture into meso-scale aeolian transport models. To facilitate model setup and the use of this surface moisture model, the soil water retention data from 10 beaches with variable grain size characteristics are provided in this study. Future studies may focus on additional model validation against data sets with variable meteorological conditions and simultaneous moisture and aeolian transport observations.

1. Introduction

Coastal dunes have important functions for flood safety, ecology, recreation, and drinking water production; but at the same time, they are commonly threatened by coastal development, sea-level rise, and erosion (Bilskie et al., 2014; Doody et al., 2004; Line et al., 2014; Nordstrom, 2000; Wong et al., 2015). The development of coastal dunes depends on an interplay of destructive and constructive forces; in simple terms, storm surges and large waves erode the dunes, and aeolian transport builds up the dunes. Previously, research efforts have primarily been put into estimating dune erosion during storm events (Kriebel and Dean, 1985; Larson and Kraus, 1989; Nishi and Kraus, 1996; Overton et al., 1988; Roelvink et al., 2009; Steetzel, 1993; Vellinga, 1986). But in recent decades, since natural processes started to play a more central role in coastal management, numerical models simulating aeolian transport and dune build-up have received increasing attention (Durán and Moore, 2013; Groot et al., 2011; Hage et al., 2020; Hoonhout and de Vries, 2016; Luna et al., 2011; Roelvink and Costas,

2019; Sauermann et al., 2001; van Dijk et al., 1999; van Rijn and Strypsteen, 2020; Zhang et al., 2015b). The challenge for these models is that the commonly used formulas for wind transport (Bagnold, 1937; Hsu, 1971; Kawamura, 1951; Lettau and Lettau, 1978; Owen, 1964; Zingg, 1953) tend to overestimate the transport rate when compared to field observations (Barchyn et al., 2014; de Vries et al., 2012; Sherman and Bauer, 1993). For realistic simulations of dune growth, supply-limiting factors, such as fetch length (Bauer et al., 2009; Delgado-Fernandez, 2010), armour layers (Nickling and Mc Kenna Neumann, 1995), grain size (Bagnold, 1937), and surface moisture (Chepil, 1956; Namikas and Sherman, 1995), need to be included in the models. In this paper, we propose a new model to predict the surface moisture on sandy beaches for aeolian transport applications.

Surface moisture content is important for aeolian transport applications because it increases the critical shear velocity for initiation of aeolian transport (Chepil, 1956). Surface moisture causes intergranular cohesion and adhesion of water particles to the sand grains. Studies that relate moisture content to thresholds for aeolian transport give a range

* Corresponding author. Faculty of Engineering, Lund University, John Ericssonsv 1, 221 00, Lund, Sweden.

E-mail address: caroline.hallin@tvrl.lth.se (C. Hallin).

<https://doi.org/10.1016/j.coastaleng.2023.104376>

Received 2 August 2022; Received in revised form 16 June 2023; Accepted 28 July 2023

Available online 29 July 2023

0378-3839/© 2023 The Authors. Published by Elsevier B.V. This is an open access article under the CC BY license (<http://creativecommons.org/licenses/by/4.0/>).

of results. In the field, volumetric moisture contents from 2 to 10% have been observed to cease aeolian transport (Delgado-Fernandez, 2010; Namikas and Sherman, 1995; Wiggs et al., 2004). Typically, lower threshold values are observed in the field compared to the laboratory; probably because saltating grains from drier areas set off the transport in the moist area (Davidson-Arnott et al., 2005; Wiggs et al., 2004). The wide range of results may partly be explained by differences in moisture observation techniques and measurement depth.

The vertical gradient in moisture content in the upper centimetres close to the surface can be steep (Edwards et al., 2013; Schmutz, 2014; Wiggs et al., 2004). Since the aeolian transport takes place at the sand surface, moisture measurements related to aeolian transport should preferably span only the upper millimeters of the sand (Uphues et al., 2022). The moisture content at the sand surface can be measured by scraping off a thin sediment layer that is weighed before and after drying. However, this gravimetric measurement technique is labour-intensive and only allows for invasive observations that are discrete in time (Edwards et al., 2013). Furthermore, scraped samples can easily be disturbed and lose moisture when transported (Paprocki et al., 2022). As an alternative, continuous *in situ* observations can be achieved with moisture probes. However, they typically penetrate 2–6 cm into the ground and can not measure the upper millimeters of the sand surface (Davidson-Arnott et al., 2005; Edwards et al., 2013). In recent years, remote sensing techniques for observations of beach surface moisture have been developed using, e.g., cameras, satellite imagery, and terrestrial laser scanners (Di Biase et al., 2021; Nolet et al., 2014; Paprocki et al., 2022; Smit et al., 2018, 2019; van der Werff, 2019). They are less accurate than the gravimetric moisture samples but allow for a more extensive spatial and temporal coverage that can provide useful information about beach surface moisture variability (Paprocki et al., 2022).

On the one hand, soil moisture processes on beaches are less complex than in other environments due to the lack of vegetation and relatively homogenous hydraulic properties of native beach sand (Namikas and Sherman, 1995). On the other hand, the beach soil moisture content is sensitive to spatially and temporally variable porosity, and governed by additional moisture processes that are not present in other terrestrial environments (Heiss et al., 2014; Paprocki et al., 2019). The most important processes and forcings are tide-, surge-, and wave-induced groundwater variations, wave runup, capillary transport, precipitation, percolation, and evaporation (Schmutz, 2014, Fig. 1). On the upper beach, the surface moisture is dominated by precipitation and evaporation, and on the lower beach, by the capillary rise from the groundwater head that fluctuates in response to the tide, surge, wave setup, and swash (Heiss et al., 2014; Horn, 2006; Schmutz, 2014). The capillary rise from groundwater can be described with a soil water retention function (SWR), relating the moisture content to the negative pressure caused by soil water suction (Tuller and Or, 2005). The tidal cycle causes alternating wetting and drying of the beach, which gives rise to hysteresis. Hysteresis implies that negative pressure due to soil water suction leads to different volumetric moisture contents depending on whether the soil is wetting or drying. The explaining mechanism is that water during a drying phase may be trapped in pore spaces as a “memory” of a previous

wetter stage. The difference between wetting and drying SWR can be significant, especially on more fine-grained beaches, where surface moisture typically also has a larger influence on aeolian transport (Schmutz, 2014).

State-of-the-art models used for soil moisture computations, e.g., HYDRUS (Šimunek et al., 1998), MARUN (Boufadel et al., 1999), and Hydrogeosphere (Therrien et al., 2010), are typically not developed for beaches. Still, they have proven to be useful also in beach settings, simulating, e.g., groundwater gradients that may cause beach surface instability (Paldor et al., 2022) and subsurface flow and moisture content in the swash zone (Geng et al., 2017). Specific models have been developed for swash zone sediment transport that simulates non-hydrostatic groundwater flow and compute vertical flow velocities in the swash zone, e.g., XBeach (McCall et al., 2014) and BeachWin (Li et al., 2002).

However, simulations of swash and vertical resolution of the soil moisture profile are unnecessary for aeolian transport applications. Instead, several aeolian transport and dune evolution models have implemented reduced complexity approaches. For example, the aeolian transport model Psamathe simulates the groundwater level and surface moisture due to tide-induced groundwater variations and capillary rise (Brakenhoff et al., 2019; Hage et al., 2020; Ruessink et al., 2022). In the cellular automata model Dubeveg (Groot et al., 2011), groundwater is included as a transport limitation. The groundwater level is not simulated within the Dubeveg model but is defined as an elevation proportional to a defined equilibrium profile, ranging from 0 to 1 (Silva et al., 2017). In another cellular automata model by Zhang et al. (2015), a moisture condition based on the daily precipitation modifies the transport mode. In the Coastal Dune Model (CDM by Durán and Moore, 2013), the threshold shear stress is modified for moist conditions depending on the distance to the groundwater table. The aeolian sediment transport and dune evolution model by van Dijk et al. (1999), multiplies the threshold velocity by correction factors to account for relative humidity and precipitation. However, none of the existing aeolian transport models includes all the relevant moisture processes to describe beach surface moisture from the waterline to the dune toe, as identified in the fundamental work by Schmutz (2014).

This study proposes a model dedicated to simulating surface moisture content for aeolian transport simulations with coastal engineering applications. Included processes are tide and wave-induced groundwater variations, wave runup, capillary rise with hysteresis, percolation, precipitation, and evaporation. The new surface moisture model is integrated into the process-based aeolian transport model AeoliS (Hoonhout and de Vries, 2016). The model is tested against surface moisture data from a beach in Noordwijk in the Netherlands, sampled with a novel instrument that allows for the extraction of 2 mm thick increments of the sand surface (van IJzendoorn et al., 2022). The soil water retention curve is experimentally established from four samples from the study site. Soil water retention data from additionally 10 beaches in Sweden and the Netherlands with different sediment properties are provided in Appendix C to facilitate the model application at other sites.

The next section explains the surface moisture model and outlines the equations for the included processes. The model functionality is illustrated with a demonstration case. After that, the model is applied to the case study, including a sensitivity analysis. The paper ends with a discussion and conclusion about the model result and applicability. The model code and demonstration case are available at GitHub (github.com/openearth/aeolis-python).

2 Surface moisture model

Before introducing the proposed model, some basic concepts are defined since beach groundwater and soil moisture dynamics are studied within several disciplines with varying terminology (Horn, 2002, 2006). In this study, we use the term groundwater table to describe the phreatic

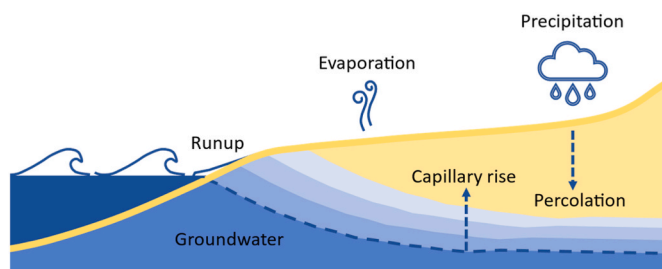


Fig. 1. Processes influencing the surface moisture on sandy beaches.

surface. The subsurface water above the groundwater table is referred to as soil water or soil moisture. The groundwater table in unconfined sandy aquifers is equivalent to the phreatic surface, where the pore water pressure equals the atmospheric pressure. The groundwater table divides the phreatic zone with positive pore pressures from the vadose zone with negative pore pressures. The vadose zone is sometimes called the unsaturated zone. A capillary fringe may develop between the groundwater table and the unsaturated zone, where the soil is saturated while pore pressures are negative.

A surface moisture model designed for aeolian transport simulations with coastal engineering applications requires specific domains and resolutions. In the vertical, the surface moisture content is simulated within a thin layer ($\Delta z \approx 2$ mm) at the beach surface (Fig. 2). This layer represents the active layer for aeolian transport, a few grain sizes thick. The horizontal model domain ranges from the water line to the dune foot. The spatial resolution in the horizontal plane is in the order of 1 m, and the temporal resolution is 10 min to an hour. The model can be applied in 1D, cross-shore transects (x-direction), or 2D, horizontal grid (x- and y-direction).

The structure of the surface moisture module and included processes are schematized in Fig. 3. The resulting surface moisture is obtained by selecting the largest of the moisture contents computed with the water balance approach (right column) and due to capillary rise from the groundwater table (left column). The proposed method is based on the assumption that the flow of soil water is small compared to the flow of groundwater and that the beach groundwater dynamics primarily is controlled by the water level and wave action at the seaward boundary (Raubenheimer et al., 1999; Schmutz, 2014). Thus, there is no feedback between the processes in the right column of Fig. 3 and the groundwater dynamics described in the left column.

2.1. Runup and wave setup

The runup height and wave setup are computed using the Stockdon formulas (Stockdon et al., 2006). Their parameterization differs depending on the dynamic beach steepness expressed through the Irribaren number,

$$\xi = \tan \beta / \sqrt{H_0/L_0} \quad (1)$$

where H_0 is the significant offshore wave height, L_0 is the deepwater wavelength, and $\tan \beta$ is the foreshore slope.

For dissipative conditions, $\xi < 0.3$, the runup, R_2 , is parameterized as,

$$R_2 = 0.043 \sqrt{H_0 L_0} \quad (2)$$

and the wave setup as,

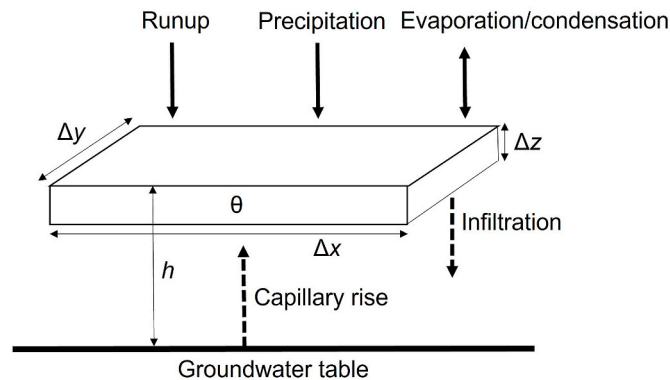


Fig. 2. Processes influencing the volumetric moisture content θ at the beach surface in a grid cell with the dimensions $\Delta x \Delta y \Delta z$ located h centimetre above the groundwater table.

$$\langle \eta \rangle = 0.02 \sqrt{H_0 L_0} \quad (3)$$

For $\xi > 0.3$, runup is parameterized as,

$$R_2 = 1.1 \left(0.35 \tan \beta \sqrt{H_0 L_0} + \frac{\sqrt{H_0 L_0 (0.563 \tan^2 \beta + 0.004)}}{2} \right) \quad (4)$$

The wave setup is,

$$\langle \eta \rangle = 0.35 \xi \quad (5)$$

2.2. Tide- and wave-induced groundwater variations

Groundwater flow under sandy beaches can be considered as flow in shallow aquifers, with only horizontal groundwater flow so that the pressure distribution is hydrostatic (Baird et al., 1998; Brakenhoff et al., 2019; Nielsen, 1990; Raubenheimer et al., 1999). The cross-shore flow dominates temporal variations of groundwater levels. Alongshore, groundwater table variations are typically small (Schmutz, 2014). Therefore, the groundwater simulations are performed for 1D transects cross-shore to ensure numerical stability at the seaward boundary and reduce computational time.

The beach aquifer is schematized as a sandy body, with saturated hydraulic conductivity, K , and effective porosity (or specific yield), n_e . The aquifer is assumed to rest on an impermeable surface, where D is the aquifer depth. The groundwater elevation relative to the mean sea level (MSL) is denoted η , and the shore-perpendicular x-axis is positive landwards, with an arbitrary starting point. The sand is assumed to be homogenous and isotropic. In this context, isotropy implies that hydraulic conductivity is independent of flow direction.

The horizontal groundwater discharge per unit area, u , is then governed by Darcy's law,

$$u = -K \frac{\partial \eta}{\partial x} \quad (6)$$

and the continuity equation (see e.g., Nielsen, 2009),

$$\frac{\partial \eta}{\partial t} = -\frac{1}{n_e} \frac{\partial}{\partial x} ((D + \eta)u) \quad (7)$$

where t is time.

At beaches, the infiltration of wave runup increases the groundwater level locally (Nielsen et al., 1988). In field experiments, rapid changes in the groundwater table have been observed over swash cycles, especially when a capillary fringe is present close to the sand surface (Heiss et al., 2014, 2015; Turner and Nielsen, 1997). The soil moisture dynamics at the timescale of swash cycles are important for, e.g., chemical groundwater dynamics and hydraulic sediment transport. However, the swash zone is too wet for aeolian transport, and simplified approaches can be applied to predict the time-averaged effect of swash on the groundwater table (Brakenhoff et al., 2019).

In a field experiment on beaches north of Sydney, Australia, it was found that when comparing two beaches with the same tidal regime, the beach that was exposed to waves had a groundwater table that was locally up to 0.7 m higher compared to the sheltered beach (Kang et al., 1994). The groundwater overheight due to runup, U_i , is computed by (Kang et al., 1994; Nielsen et al., 1988),

$$U_i = \begin{cases} C_l K f(x) & \text{if } x_S \leq x \leq x_R \\ 0 & \text{if } x > x_R \end{cases} \quad (8)$$

where C_l is an infiltration coefficient (–), and $f(x)$ is a function of x ranging from 0 to 1. x_S is the horizontal location of the intersection between the beach face and the still water level, including wave setup. x_R is the horizontal location of the runup limit.

Different forms of the equation $f(x)$ have been proposed, e.g., negative exponential (Nielsen et al., 1988) and linearly increasing

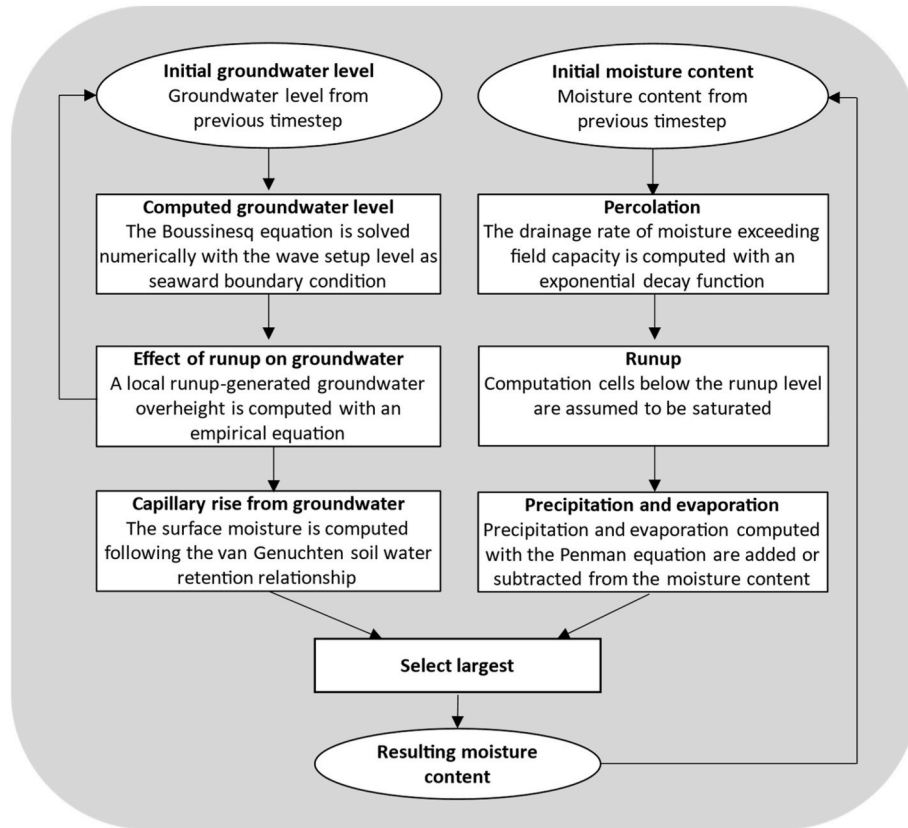


Fig. 3. Implementation of the surface moisture processes in the model.

(Brakenhoff et al., 2019) with distance to the shoreline. When compared to field data, Kang et al. (1994) found that $f(x)$ had a maximum at $x = 2/3(x_{ru}-x_s)$. The distribution likely depends on several factors, e.g., the moisture content, the hydraulic conductivity (which also depends on the moisture), and the distribution of runup. We propose the following linear equations for $f(x)$, with a maximum of 1 at $x = 2/3(x_{ru}-x_s)$ and 0 at x_{ru} and x_s ,

$$f(x) = \begin{cases} \frac{x - x_s}{\frac{2}{3}(x_{ru} - x_s)} & \text{if } x_s < x \leq x_s + \frac{2}{3}(x_{ru} - x_s) \\ 3 - \frac{x - x_s}{\frac{1}{3}(x_{ru} - x_s)} & \text{if } x_s + \frac{2}{3}(x_{ru} - x_s) < x < x_{ru} \end{cases} \quad (9)$$

Substitution of u (equation (5)) in the continuity equation (equation (6)) with the addition of U_l/n_e gives the nonlinear Boussinesq equation,

$$\frac{\partial \eta}{\partial t} = \frac{K}{n_e} \frac{\partial}{\partial x} \left((D + \eta) \frac{\partial \eta}{\partial x} \right) + \frac{U_l}{n_e} \quad (10)$$

The Boussinesq equation is solved numerically with a central finite difference method in space and a fourth-order Runge-Kutta integration technique in time (see, e.g. Brakenhoff et al., 2019; Liu and Wen, 1997; Schmutz, 2014; Raubenheimer et al., 1999). The numerical solution is detailed in Appendix A.

The seaward boundary condition is defined as the still water level plus the wave setup (Raubenheimer et al., 1999). If the groundwater elevation is larger than the bed elevation, the groundwater elevation is set equal to the bed elevation (Baird et al., 1998). On the landward boundary, either a no-flow condition, $d\eta/dx = 0$ (Neumann condition), or constant head, $\eta = \text{constant}$ (Dirichlet condition), can be prescribed (Brakenhoff et al., 2019; Raubenheimer et al., 1999).

2.3. Capillary rise

SWR functions describe the surface moisture due to capillary transport of water from the groundwater table. The resulting surface moisture is computed for both drying and wetting conditions, i.e., including the effect of hysteresis. An effective saturation S_e is defined as,

$$S_e = \frac{\theta - \theta_r}{\theta_s - \theta_r} \quad (11)$$

where θ is the volumetric moisture content; θ_r is the residual moisture content due to water being trapped in pores or otherwise so strongly held that it is unavailable for flow, and θ_s is the moisture content at atmospheric pressure, i.e., the saturated moisture content.

A commonly used and widely accepted relationship between the effective saturation and soil water suction is the one proposed by van Genuchten (1980) (Brakenhoff et al., 2019; Schmutz, 2014; Zhu, 2007),

$$S_e = (1 + (ah)^n)^{-m} \quad (12)$$

where h is the groundwater table depth, α and n are fitting parameters related to the air entry suction and the pore size distribution. The parameter m is commonly parameterised as $m = 1-1/n$. Substituting the equation for effective saturation into van Genuchten's equation and solving for the moisture content as a function of matric suction, $\theta(h)$, yields,

$$\theta(h) = \theta_r + \frac{\theta_s - \theta_r}{[1 + |ah|^n]^m} \quad (13)$$

The moisture contents computed with drying and wetting SWR functions are denoted $\theta^d(h)$ and $\theta^w(h)$, respectively (an example of drying and wetting SWR functions can be seen in Fig. 11). When moving between wetting and drying conditions, the soil moisture content can be described with an intermediate SWR function called a scanning curve.

The drying scanning curves are scaled from the main drying SWR function and wetting scanning curves from the main wetting SWR function. For engineering purposes, [Pham et al. \(2005\)](#) recommend the method Mualem model II to derive the scanning curves. The drying scanning curve is then obtained from ([Mualem, 1974](#)):

$$\theta^d(h_{\Delta}, h) = \theta^w(h) + \frac{[\theta^w(h_{\Delta}) - \theta^w(h)]}{[\theta_s - \theta^w(h)]} [\theta^d(h) - \theta^w(h)] \quad (14)$$

where h_{Δ} is the groundwater table depth at the reversal on the wetting curve.

The wetting scanning curve is obtained from ([Mualem, 1974](#)):

$$\theta^w(h_{\Delta}, h) = \theta^w(h) + \frac{[\theta_s - \theta^w(h)]}{[\theta_s - \theta^w(h_{\Delta})]} [\theta^d(h_{\Delta}) - \theta^w(h_{\Delta})] \quad (15)$$

where h_{Δ} is the groundwater table depth at the reversal on the drying curve.

The resulting surface moisture due to capillary rise is determined by selecting the largest of $\theta^w(h)$ and $\theta^w(h_{\Delta}, h)$ during wetting conditions (rising groundwater levels) and the smallest of $\theta^d(h)$ and $\theta^d(h_{\Delta}, h)$ during drying conditions (falling groundwater levels).

Sometimes there is a reversal between wetting and drying conditions while the moisture content is computed with a scanning curve. In that case, the moisture content is computed from the other scanning curve in the consecutive timestep. If the moisture content is computed from a wetting scanning curve when there is a reversal to drying conditions, an equivalent $h_{\Delta, h_{\Delta, eq}}$ is solved from the drying scanning curve for which $\theta^d(h_{\Delta, eq}, h) = \theta^w(h_{\Delta}, h)$, and vice versa if there is a reversal on the drying scanning curve.

2.4. Percolation

Percolation is accounted for by assuming that excess water drains until the moisture content reaches field capacity, θ_{fc} . The moisture content at field capacity is the maximum amount of water that the unsaturated zone of soil can hold against the pull of gravity. For sandy soils, the matric potential at this soil moisture condition is around -1/10 bar. In equilibrium, this potential would be exerted on the soil capillaries at the soil surface when the water table is about 100 cm below the soil surface, $\theta_{fc} = \theta^d(100)$.

The percolation rate is assumed to follow an exponential decay function,

$$\frac{d\theta}{dt} = (\theta - \theta_{fc}) \left(e^{-\ln(2) \frac{t}{T_{dry}}} \right) \quad (16)$$

where T_{dry} is the time it takes for half of the excess moisture content, $\theta - \theta_{fc}$, to drain.

2.5. Precipitation and evaporation

A water balance approach accounts for the effect of precipitation and evaporation,

$$\frac{d\theta}{dt} = \frac{(P - E)}{\Delta z} \quad \theta_r \leq \theta \leq \theta_s \quad (17)$$

where P is the precipitation, E is the evaporation, and Δz is the thickness of the surface layer. Evaporation is computed with the Penman equation following the method outlined in [Shuttleworth \(1993\)](#) (see [Appendix B](#)).

2.6. Demonstration case

To demonstrate the functionality of the surface moisture model, the model is applied to a simple test case. The test case consists of a 1 D profile with a uniform slope of 1:100 ([Fig. 4a](#)). The profile is exposed to a semi-diurnal tide with a 2 m range and constant waves with 1 m wave height and 5 s period ([Fig. 4c](#)). The hydraulic properties of the sand are taken from a study at a beach with a mean grain size of 0.13 mm ([Schmutz, 2014](#)): $\theta_r = 0.09 \text{ m}^3/\text{m}^3$, $\theta_s = 0.4448 \text{ m}^3/\text{m}^3$, $n = 4.931$, $m = 0.797$, $K = 8.5 \times 10^{-5} \text{ m/s}$, $\alpha_d = 0.019 \text{ cm}^{-1}$, and $\alpha_w = 0.034 \text{ cm}^{-1}$. The meteorological properties are constant with 20 °C air temperature, 1013 kPa air pressure, 70 MJ/m²/d global radiation, 70% relative humidity, and 10 m/s wind speed. After 20 h, there is a 2 mm/h rainfall with 2 h duration.

The results show that at the cross-shore location at 0 m above MSL, the moisture content of the beach is constantly saturated ([Fig. 4b](#)). The surface moisture at 0.8 and 1 m above MSL fluctuates with the tide, but the more seaward location is wetter. The jump in the 1 m curve when moving from drying to wetting conditions occurs due to a shift from the drying to the wetting SWR curve. During the rising tide, the surface moisture responds faster than during the falling tide. The groundwater table drops slower than the water level at the seaward boundary and results in a decoupling that is typical for beach groundwater ([Fig. 4a](#); see, e.g., [Horn \(2006\)](#)). Additionally, at the same matric suction in the unsaturated zone, more soil water is being held during drying conditions than during wetting conditions.

At the most landward cross-shore location at 2 m above MSL, the surface moisture is not influenced by the beach groundwater. It is constantly equal to the residual moisture content except during the rainfall and subsequent drying.

3. Field site and data

Noordwijk beach is located on the Holland coast in the Netherlands ([Fig. 5](#)). The beach has a mean tidal range of 1.6 m and a spring tide range of 1.8 m ([Wijnberg, 2002](#)), and during storm surges, the water level reaches about 2–4 m above MSL ([Baart et al., 2011](#)). The annual mean significant deepwater wave height is about 1 m, and storm wave

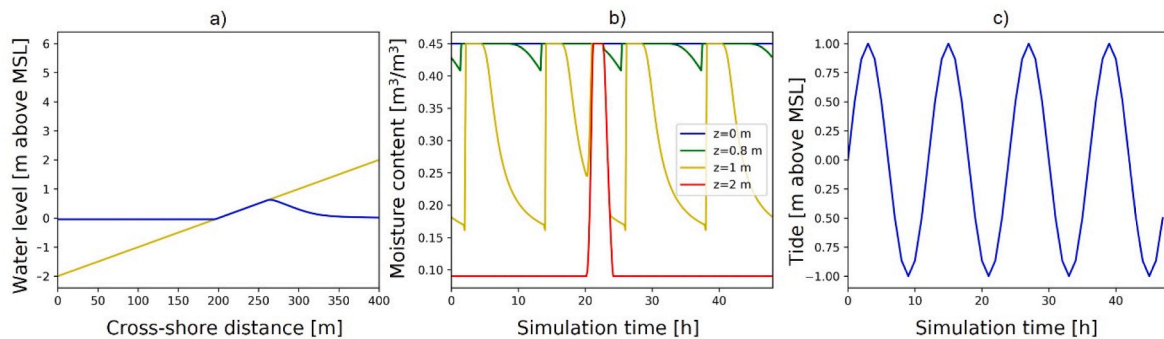


Fig. 4. Result of demonstration case showing: a) Tide and groundwater level at $t = 35$ h. b) The surface moisture content at four different cross-shore locations with bed levels 0, 0.8, 1, and 2 m above MSL. After 20 h, there is a rainfall of 2 mm/h and 2 h duration. c) Tide during simulation.

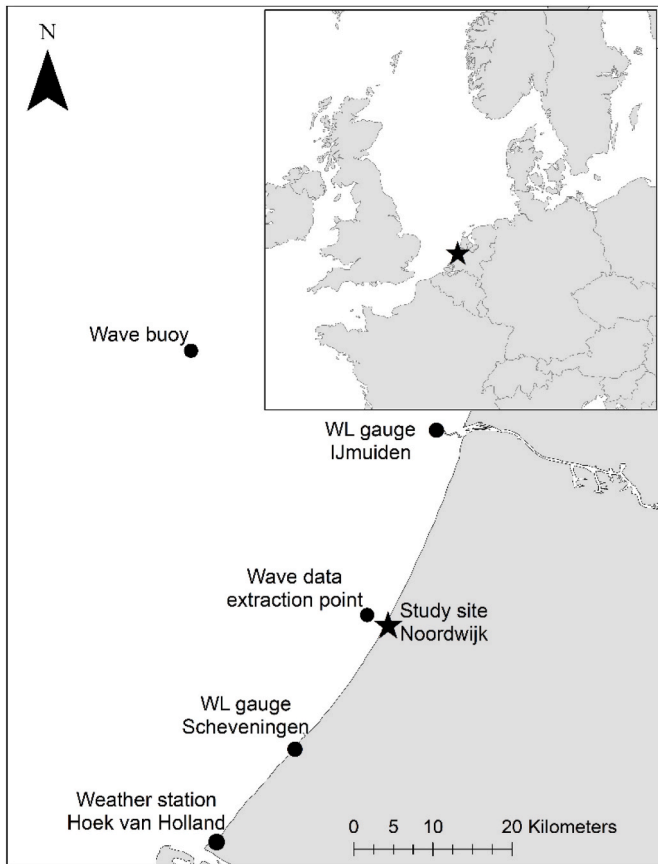


Fig. 5. Overview map of the study area with wave buoy, wave data extraction point from wave model, water level (WL) gauges, and weather station.

heights reach 5 m (Wijnberg, 2002).

Since 1990, the beach in Noordwijk has been nourished with approximately $1000 \text{ m}^3/\text{m}$, mostly as shoreface nourishments and partly as beach nourishments (Brand et al., 2022). The Holland coast has a negative sediment budget and was eroding during the last 2000 years until the coast was stabilised by nourishments (Stive et al., 1990). Currently, the beach has an approximate width of 100–150 m, and the dune toe is located at about 3 m above MSL (van IJzendoorn et al., 2021). It has a dynamic bar behaviour with bar cycling and switching (Ojeda et al., 2008; Wijnberg and Terwindt, 1995). The intertidal zone is occasionally characterised by ridge and runnel morphology (Fig. 6). The beach sand is medium-sized and influenced by the nourishments (Wijnberg, 2002). Fig. 7 displays a characteristic grain size distribution



Fig. 6. Study site at Noordwijk beach on 24 March 2020. Photo: Christa van IJzendoorn.

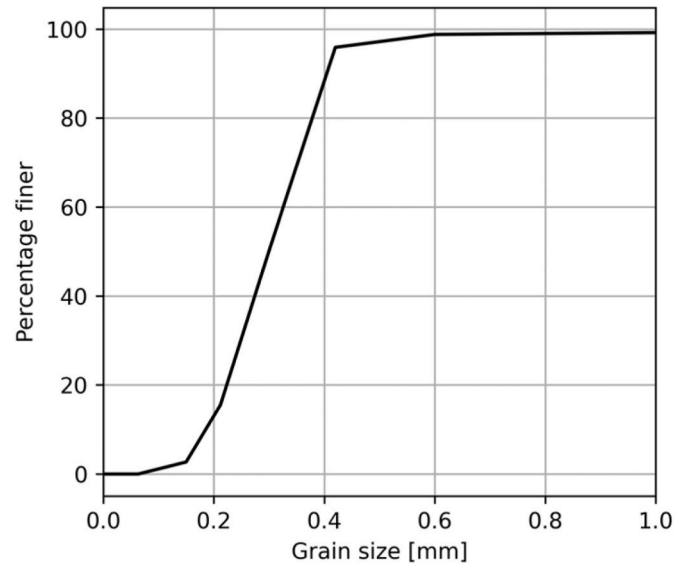


Fig. 7. Typical grain size distribution from the study site.

from the study site with a median grain size, D_{50} , of 0.3 mm (van IJzendoorn et al., 2022).

3.1. Surface moisture observations

The surface moisture was measured in 221 sediment samples from the upper 2 mm distributed over an area measuring approximately $100 \times 200 \text{ m}$ (Fig. 8). The samples were spread out in time during three sampling occasions; 30 January 2020 (8 a.m.–3 p.m.; 74 samples), 24 March 2020 (8 a.m.–3 p.m.; 73 samples), and 24 April 2020 (9 a.m.–3 p.m.; 74 samples).

The samples were collected using a sand scraper with a dialling mechanism that allows sampling with 2 mm depth increments (van IJzendoorn et al., 2022). The samples covered an area of 0.04 m^2 and had a dry weight of about 150 g. The samples were collected in sealed plastic bags and weighed before and after they were oven-dried at $100 \text{ }^\circ\text{C}$. The gravimetric moisture content, w [kg/kg], i.e., the percentage of water mass divided by the dry mass of the soil, was converted to volumetric moisture content, θ [m^3/m^3], i.e., the percentage of water volume divided by the volume of the soil, by,

$$\theta = \frac{w\rho_b}{\rho_w} \quad (18)$$

where ρ_w [kg/m^3] and ρ_b [kg/m^3] are the water and bulk density, respectively. It was assumed that $\rho_w = 1025 \text{ kg}/\text{m}^3$. The volumetric moisture content in the samples was distributed between 0.0017 and $0.40 \text{ m}^3/\text{m}^3$ with an average of $0.20 \text{ m}^3/\text{m}^3$ and a standard deviation of $0.11 \text{ m}^3/\text{m}^3$ (Fig. 9).

The grain sizes of the samples from Noordwijk were determined by dry sieving with ten sieve screens ranging from 0.063 mm to 3.350 mm, based on British Standard BS1377-2 (1990). The average D_{50} was about 0.29 mm, with a standard deviation of 0.04 mm. The 10th and 90th quantiles, D_{10} and D_{90} , were 0.18 and 0.44 mm on average, with standard deviations of 0.03 and 0.06 mm, respectively. The grain size samples showed considerable spatial variations, with the D_{50} of samples varying between 0.2 and 0.5 mm. Coarser sand was found on the landward side of the runnel related to the presence of sand bars (Fig. 6), but the samples did not display a clear cross-shore trend.

In addition, six vertical profiles with samples at 2, 4, 8, 14, 20, 26, 32, 38, 44, and 50 mm soil depth were collected on 5 February 2020 and analysed with the same methods. The average moisture content of these samples was $0.25 \text{ m}^3/\text{m}^3$ and a standard deviation of $0.10 \text{ m}^3/\text{m}^3$. The

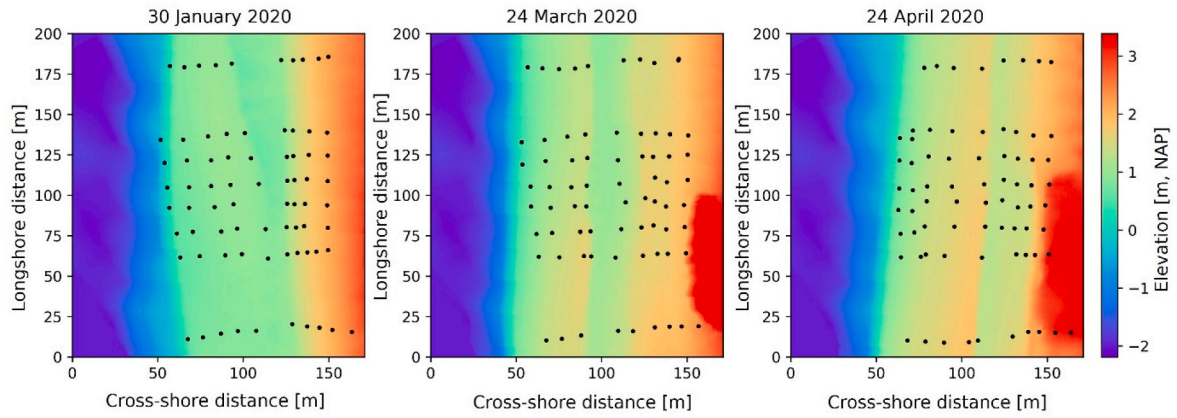


Fig. 8. Digital elevation models from the study area at the different sampling occasions. Sample points are marked with black circles.

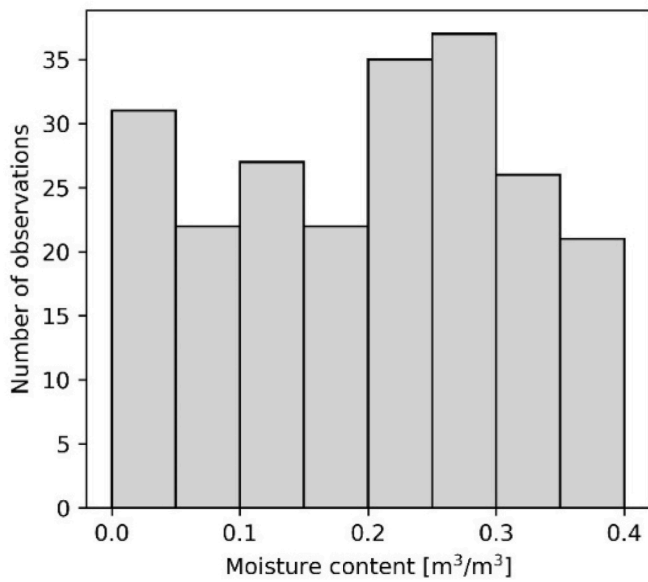


Fig. 9. Histogram of surface moisture observations.

grain size and moisture content were normalized against the average values within each vertical profile. Within this depth range, 0–5 cm, there was a weak negative correlation ($R^2 = 0.08$; <5% significance level) between sample depth and moisture content (Fig. 10). However,

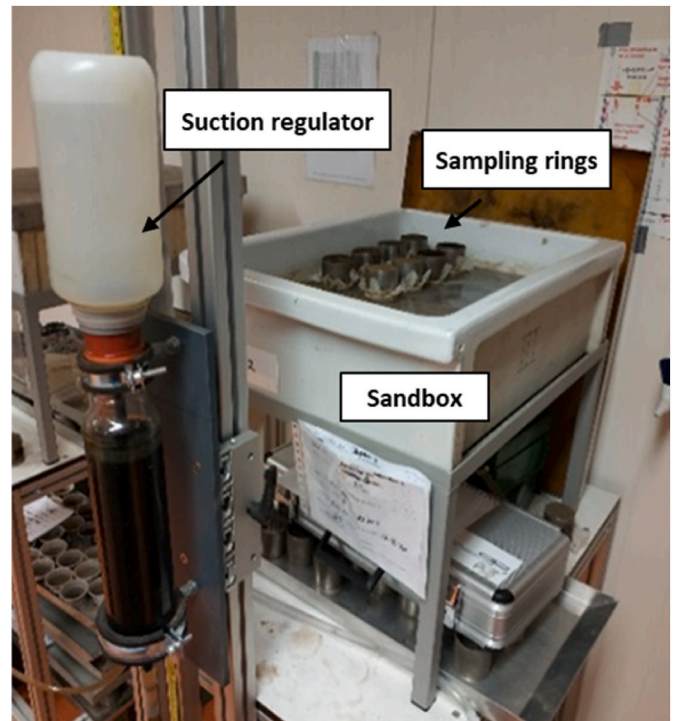


Fig. 11. Setup of the sandbox experiment.

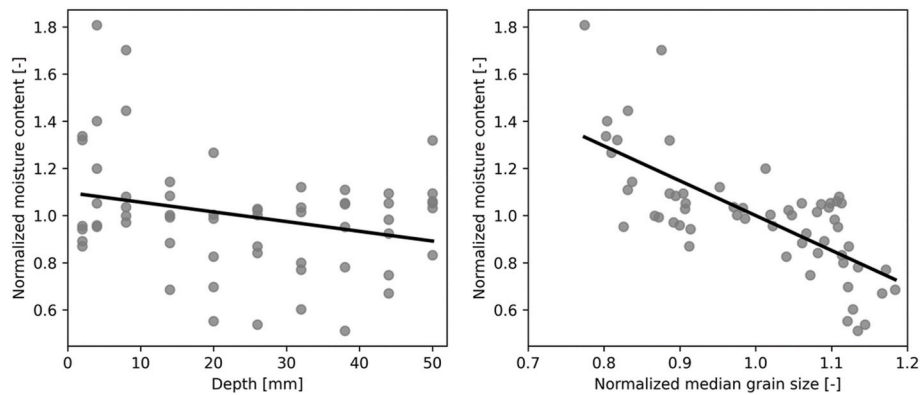


Fig. 10. Normalized moisture content from vertical sampling profiles plotted against sample soil depth (left panel) and normalized median grain size (right panel). The moisture content and median grain size were normalized by dividing the value of each sample by the average value of the vertical set of samples to which they belong.

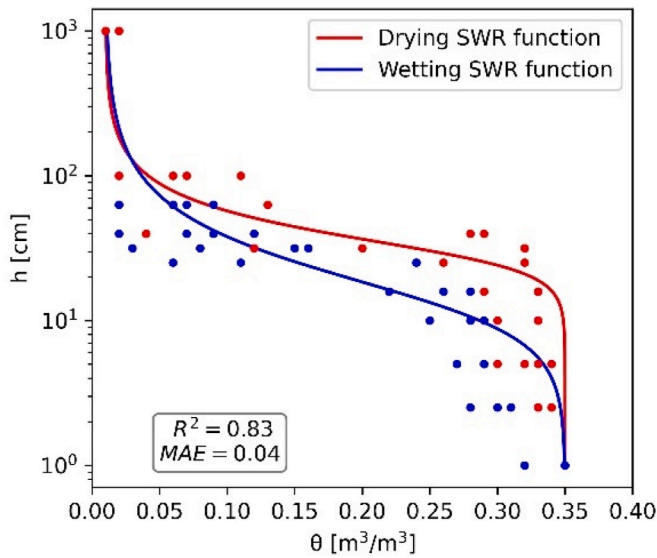


Fig. 12. Drying and wetting soil water retention functions fitted to the observations from the sandbox experiment.

moisture content had a stronger negative correlation ($R^2 = 0.51$; <1% significance level) with the grain size (Fig. 10). The samples from >2 mm depth are not included in the model evaluation and are only presented here to illustrate the grain size and moisture variability in surface sediments.

3.2. Bathymetry and topography

For each sampling occasion, digital elevation models (DEMs) with 1×1 m resolution were constructed based on data from a Terrestrial Laser Scanner (TLS). The TLS Riegl VZ-2000 has a vertical accuracy of 8 mm and was mounted on top of a building about 200 m behind the beach (Di Biase et al., 2021; Vos et al., 2017). The TLS point clouds had a density of approximately 9 points/m² and were measured during low tide. The point clouds were corrected based on georeferenced points in the field of view of the laser scanner and cleaned manually to remove disturbances (e.g., vehicles, humans). Subsequently, a DEM was made of the TLS point cloud and combined with bathymetry from a JARKUS grid measured in 2020 (Rijkswaterstaat, 2020). The transition between the bathymetry and DEM was smoothed by applying a 10×10 m moving average window to the area within 20 m of the boundary. To align with the coastline, the DEMs were rotated 30° counter-clockwise and resampled to a local 1×1 m grid with origin in N 52.24222°, E 4.42235° (Fig. 8). The elevation is presented relative to Dutch Ordnance Datum (NAP), which is approximately equal to the mean sea level.

The intertidal area of the study site has a dynamic morphology. A ridge and runnel system is present on all sampling occasions. The runnel was filled with water during the last two sampling occasions, 24 March 2020 and 24 April 2020 (Fig. 6 display a photo of the runnel on 24 March 2020).

3.3. Soil hydraulic properties

On 9 November 2020, two sets of duplicate soil samples were collected on the study site at N 52.24204°, E 4.42428° and N 52.24240°, E 4.42460° using a sampling ring of 100.14 cm³, sampling to 5.1 cm soil depth from the beach surface. The bulk densities of the samples ranged from 1.58 to 1.65 g/cm³. The drying and wetting curves of soil water retention were determined using a sandbox experiment (Fig. 11), set up according to the method outlined by Dirksen (1999). The sampling rings containing the soil were placed in a box on top of synthetic wetted sand covered with a filter cloth. The box was connected through a tube

Table 1
Weather data during the sampling dates, average values, and minimum and maximum values range. During the first sampling occasion, precipitation occurred in the last hour, at 3 p.m.

Sampling date	Temperature [°C]	Global radiation [MJ/m ² /d]	Precipitation [mm/h]	Air pressure [kPa]	Relative humidity [%]	Wind speed [m/s]
30 January 2020 8 a.m.–3 p.m.	7.8 (6.2–8.9)	9.6 (0.5–20.6)	0.1 (0–1.1)	1005.8 (1001.9–1008.8)	86.8 (81–98)	8.8 (7–10)
24 March 2020 8 a.m.–3 p.m.	10.5 (5.7–12.8)	46.4 (22.1–58.3)	0	1029.7 (1028.0–1031.1)	28.6 (22–44)	6.8 (6–8)
24 April 2020 9 a.m.–3 p.m.	13.0 (12.5–13.4)	60.2 (49.4–69.6)	0	1015.3 (1014.8–1015.6)	71.3 (68–75)	5.5 (5–7)

to an adjustable steady water head (suction regulator). When the water level was below the reference level for the samples, suction was applied to the samples. The amount of suction corresponded to the difference between the middle of the soil sample and the water head. For deriving the drying curve, the suction was stepwise increased from 0 pF to 2 pF, while for the wetting curve, the suction was decreased from 2 pF to 0 pF.

After each increment, the samples were weighed to record the wet weight of the soil at the respective water head. Once the measurements were finalised, all samples were oven-dried at 105 °C for more than 24 h to determine the dry weight of the soil. Finally, the wet weight of the disturbed soil samples at a pressure potential of pF 3.0 was estimated using a pressure plate.

Per sample, the gravimetric moisture content w [kg/kg] corresponding to the different pressure potentials (pF 0–3, wetting and drying) was calculated and converted to volumetric moisture content θ [m^3/m^3].

Soil water retention functions (SWR) of the van Genuchten-type were fitted to the observations from the sandbox experiment (Fig. 12). The residual and satiated moisture content were determined by the minimum and maximum volumetric moisture content. The wetting SWR did not converge when all the other parameters were free; instead, m was defined by the commonly used relationship $m = 1 - 1/n$. The fitted van Genuchten parameters for the drying (d) and wetting (w) conditions, respectively, were, $\theta_r = 0.01 \text{ m}^3/\text{m}^3$, $\theta_s = 0.35 \text{ m}^3/\text{m}^3$, $\alpha^d = -0.035$, $\alpha^w = -0.070$, $n^d = 4.5$, $n^w = 2.3$, and $m^d = 0.42$.

3.4. Weather, waves, and water levels

Weather data with an hourly resolution, consisting of temperature, global radiation, precipitation, air pressure, relative humidity, and wind speed, were collected from the weather station at Hoek van Holland (KNMI, 2022) (Fig. 5). The weather data during the sampling periods are summarized in Table 1.

Water levels were taken as the average value of observations with 10 min frequency from the gauges in IJmuiden Stroometpaal and Scheveningen operated by Rijkswaterstaat (2022) (Figs. 5 and 13).

Deepwater significant wave height, period, and direction were collected from an offshore wave buoy (Fig. 5) and transformed towards the coast using a SWAN wave model (Booij et al., 1999) for the Holland coast. Nearshore transformed waves - significant wave height, period, and direction - were extracted at 14 m depth (Fig. 5). Only the onshore component of wave energy was accounted for in the runup and setup equations according to $H_0 = H'_0 \sqrt{\cos \varphi}$, where H'_0 is the non-corrected wave height, H_0 is the wave height representing the onshore energy flux, and φ is the offshore incident wave angle from the shore normal (Hanson and Larson, 2008) (Fig. 13).

4. Model setup and evaluation

The topographic data, forcing, and soil hydraulic parameters were based on the data described in the previous section. Based on geological maps, the aquifer depth under the beach was estimated to be 12 m (TNO, n.d.). The effective porosity, n_e , was set to the commonly assumed value of $n_e = 0.3$. The saturated hydraulic conductivity, K , was calibrated to $K = 2 \times 10^{-4} \text{ m/s}$. The dimensionless infiltration coefficient, Cl , was set to generate a groundwater table overheight of about 0.2 m. The landward boundary condition for the groundwater model was set as a no-flow (Neumann) condition. The drying timescale for the percolation, T_{dry} , was set to 1.5 h. The water-filled runnels that were present on the beach during the two last sampling occasions, 24 March 2020 and 24 April 2020, were implemented as a static head of +1.1 m (relative NAP) and +1.35 m (relative NAP), respectively.

The model was set up for a rectangular area, measuring 200 m in the longshore direction and 170 m in the cross-shore direction (Fig. 8). The initial groundwater level was set to 1 m over the entire model domain, and the model was run for 8 days prior to the sampling dates to warm up. The landward boundary was set back 200 m to avoid influence on the groundwater levels within the model domain. The computational grid had a resolution of $1 \times 1 \text{ m}$, and the time step was 1 min with an output of results every 10 min. The timestep in the groundwater module was increased 30 times to assure numerical stability. The input data had a temporal resolution of 10 min for the water level data, 1 h for the meteorological data, and 3 h for the wave data.

The model's predictive capability was evaluated based on the coefficient of determination, R^2 , the Brier Skill Score, BSS, the mean error, ME, and the mean absolute error, MAE, defined according to,

$$R^2 = 1 - \frac{\sum_{i=1}^n (m_i - c_i)^2}{\sum_{i=1}^n (m_i - \bar{m})^2} \quad (19)$$

$$BSS = 1 - \frac{\sum_{i=1}^n (c_i - m_i - (\bar{c} - \bar{m}))^2}{\sum_{i=1}^n (m_i - \bar{m})^2} \quad (20)$$

$$ME = \frac{1}{n} \sum_{i=1}^n (m_i - c_i) \quad (21)$$

$$MAE = \frac{1}{n} \sum_{i=1}^n |m_i - c_i| \quad (22)$$

where c is the computed value, m is the measured value, and n is the sample size.

R^2 describes the proportion of the measured variability that the

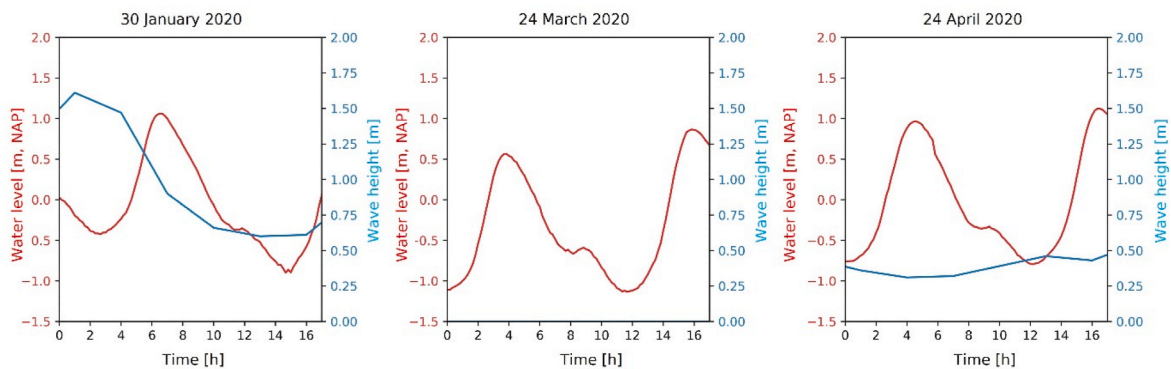


Fig. 13. Water levels and wave heights (corrected for their angle against shore-normal). On 24 March 2020 (mid panel), the waves were offshore directed and are therefore not included in the plot.

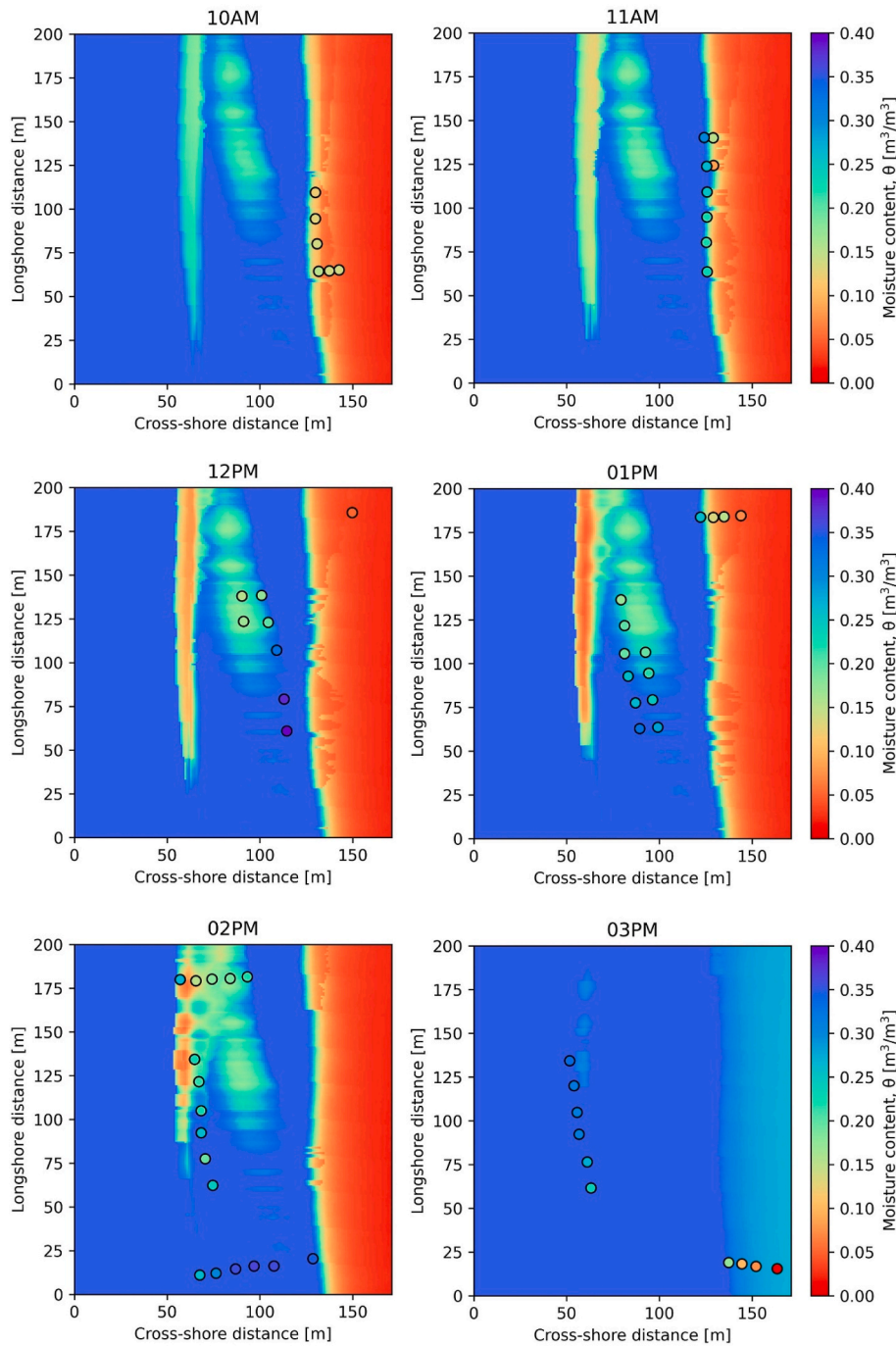


Fig. 14. Simulated (colour map) and observed (circles) surface moisture content from 10 a.m. to 3 p.m. on 30 January 2020.

model explains. $R^2 = 1$ means that all variability in the data is described by the model, i.e., a perfect fit. BSS relates the variance of the difference between the measured and modelled values to the variance of the measured values. $BSS = 1$ means perfect skill, and $BSS = 0$ means no skill. ME and MAE describe the average difference and the average absolute difference between the computed and measured values.

5. Results

The observed and simulated surface moisture display a large spatial variability within the model area. Fig. 14 illustrates the simulated and observed surface moisture during the falling tide every full hour between 10 a.m. and 3 p.m. on 30 January 2020. The model results reflect

the spatial variability of the surface moisture, although there is some offset between observations and model results. The gradient in the upper intertidal area, at a cross-shore distance of about 130 m, is generally well captured. The moisture at the intertidal bar is well-described at 12 and 1 p.m. but displays more spatial offset at 2 and 3 p.m.

At 3 p.m., there is a rainfall wetting the surface. The deviations between observations and simulations around 150 m cross-shore are related to the timing of the observations and model output. The samples were collected before the rainfall started but are moved from 10 min output to the full hour in this illustration.

When visualized in scatter plots, the simulations show large deviations compared to the observations (Fig. 15). The mean absolute error ranges from 0.06 to 0.08 m^3/m^3 . The simulations of 24 March

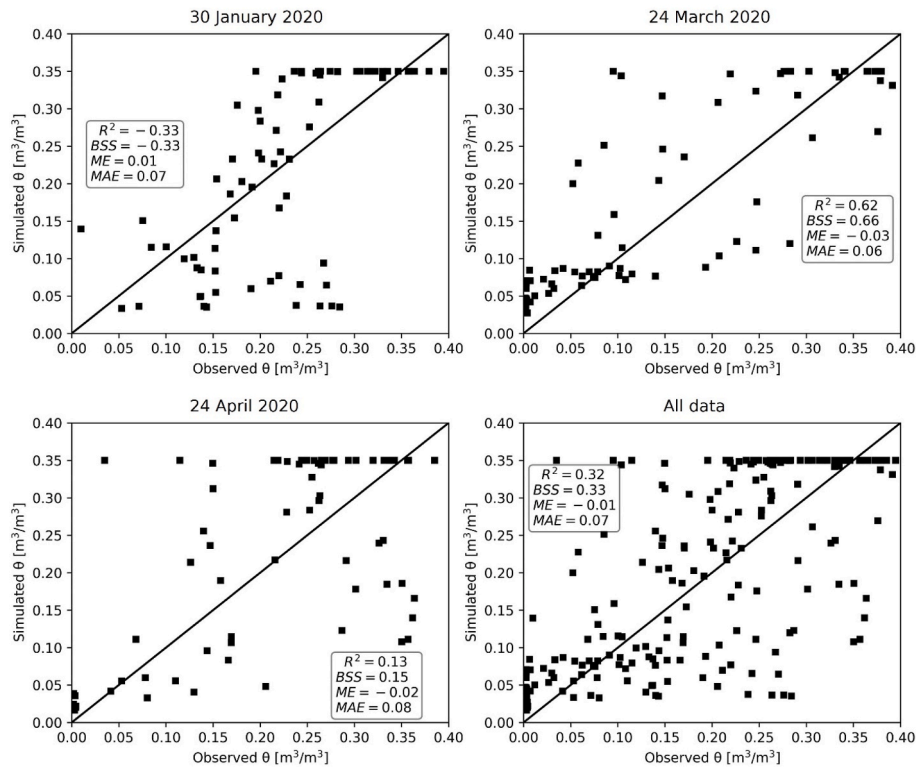


Fig. 15. Result of simulated moisture content compared to observed.

2020 and 24 April 2020 have a mean error of -0.03 and $-0.02 \text{ m}^3/\text{m}^3$, meaning that the model, on average, overestimates the moisture. On the contrary, the simulated moisture content of 30 January 2020 was drier than the observations, with a mean error of 0.01. Compared to the observations, which have an almost uniform distribution of moisture contents ranging from 0.01 to $0.40 \text{ m}^3/\text{m}^3$, the distribution of the model output overestimates the occurrence of the low ($<0.10 \text{ m}^3/\text{m}^3$) and high ($>0.30 \text{ m}^3/\text{m}^3$) moisture contents. These errors are probably related to the uncertainty and heterogeneity of the SWR relationship and the assumption of homogenous porosity.

The simulation of 24 March 2020 has the best fit to the data with $R^2 = 0.62$ and $BSS = 0.66$. The simulation of 30 January 2020 has negative values of R^2 and BSS, indicating that a random distribution of the simulated values would give a better result than the model. The model reproduces the gradient from dry to wet, but since the moisture content is underestimated for the drier observations ($<0.20 \text{ m}^3/\text{m}^3$) and overestimated for the wetter observations ($>0.20 \text{ m}^3/\text{m}^3$), the fit remains poor. For observed moisture contents below which aeolian transport could occur, $<0.10 \text{ m}^3/\text{m}^3$, the model predicts contents $<0.10 \text{ m}^3/\text{m}^3$ in 79% of the cases. The model sometimes predicts moisture contents $<0.10 \text{ m}^3/\text{m}^3$ for observations $>0.10 \text{ m}^3/\text{m}^3$, this especially occurred in the first simulation from 30 January 2020 (Figs. 14 and 15).

5.1. Sensitivity analysis

The model's sensitivity to parameter settings and included processes was investigated in a sensitivity analysis. The sensitivity analysis is summarized in Table 2 and compared to the performance of all models. The model was most sensitive to changes related to the soil water retention function and to excluding the runnel from the model setup.

Overall, the sensitivity analysis indicates that the model is stable and that small changes to the parameter setting have a limited influence on the model output. This is important for engineering applications with commonly limited access to data.

6. Discussion

This study proposes a new surface moisture model including all processes that have been identified as relevant drivers for soil surface moisture in the fundamental work by Schmutz (2014). The proposed model includes more processes and complexity than previous surface moisture descriptions in aeolian transport models (Brakenhoff et al., 2019; de Groot et al., 2011; Durán and Moore, 2013; Hage et al., 2020; Silva et al., 2017; van Dijk et al., 1999; Zhang et al., 2015a). Still, it is less complex than many other groundwater and soil water models that

Table 2

Sensitivity analysis with evaluation of coefficient of determination, R^2 , the Brier Skill Score, BSS, the mean error, ME, and the mean absolute error, MAE. The evaluation of the model performance should be compared to the original models with $R^2 = 0.32$, $BSS = 0.33$, $ME = -0.01 \text{ m}^3/\text{m}^3$, and $MAE = 0.07 \text{ m}^3/\text{m}^3$.

Modification	R^2	BSS	ME	MAE
Hysteresis excluded (wetting SWR)	0.24	0.28	0.02	0.07
Hysteresis excluded (drying SWR)	0.29	0.33	-0.02	0.07
Increased hydraulic conductivity, $K = 10 \times 10^{-4} \text{ m/s}$ (original $2 \times 10^{-4} \text{ m/s}$)	0.31	0.33	-0.02	0.07
Decreased hydraulic conductivity, $K = 0.5 \times 10^{-4} \text{ m/s}$ (original $2 \times 10^{-4} \text{ m/s}$)	0.30	0.31	-0.01	0.07
Increase grid size $10 \times 10 \text{ m}$	0.31	0.33	0.02	0.07
Runnel excluded	0.25	0.28	0.02	0.08
Groundwater overheight due to runup 0.7 m (original 0.2 m)	0.32	0.33	-0.01	0.07

have been applied to the intertidal area (e.g., Geng et al., 2017; Li et al., 2002; McCall et al., 2014). The model complexity should ideally be a balance between an accurate representation of relevant physical processes, computational efficiency, and feasibility of model application for the specific engineering and scientific purposes.

This proposed model is intended to predict surface moisture content for aeolian transport simulations. The motivation is that the intertidal area is the wettest area on the beach but simultaneously an important source area for aeolian-transported sediment (Delgado-Fernandez, 2010; Hoonhout et al., 2015). Sediment sorting due to transport results in armour layer development on the dry beach (Hoonhout and de Vries, 2019); whereas, in the intertidal area, armour layers can be broken by hydraulic mixing in the swash zone (Hoonhout et al., 2015). Thus, simulations of dune build-up at yearly to decadal timescales may be highly dependent on realistic representations of the beach surface moisture. It is particularly important that the lower surface moisture contents ($<0.10 \text{ m}^3/\text{m}^3$) are simulated with high accuracy since aeolian transport is assumed to cease at larger moisture contents (Delgado-Fernandez, 2010). At the higher moisture contents ($>0.10 \text{ m}^3/\text{m}^3$), deviations above the transport threshold will not influence transport simulation results.

The proposed surface moisture model performed relatively well within the low range of observed surface moisture contents. The overall performance of the model was less satisfactory (Fig. 15). Although the spatial moisture gradients over the intertidal area were reflected in the model results, the large variability of the moisture content caused small spatial offsets to result in large errors. All three simulations resulted in a mean absolute error of $0.07 \text{ m}^3/\text{m}^3$. Possible explanations for these errors are related to uncertainties in the wave simulations, the distance from the study area to the weather and water level gauges, DEM accuracy and resolution, the estimated hydraulic conductivity, and other processes that are not included in the model, such as overland flow. Also, the moisture observations include errors related to sampling and transport, especially for large moisture contents close to saturation which are difficult to sample without applying suction (Paprocki et al., 2022; Stark and Brilli, 2021).

A large part of the error may be attributed to the observed heterogeneity of hydraulic properties of the beach sand that is not accounted for in the model. The surface moisture samples and the four samples used for the analysis of soil water retention displayed a large variability of hydraulic properties. This effect is likely related to small-scale variability of grain size and porosity. The moisture content within 2 mm thick layers deviated from -50% to $+80\%$ in relation to the average moisture content in a 50 mm deep soil column (Fig. 10). The surface moisture variability correlated with the grain size but not with the sample depth within the column.

Additionally, the fit of the SWR function to the data derived from the laboratory analysis resulted in an MAE of $0.04 \text{ m}^3/\text{m}^3$, which could explain a large part of the model errors. The scatter in Fig. 12 can be attributed to errors related to the analysis, compaction during transport, or actual heterogeneous sediment properties at the study site. Similar spatial variability of hydraulic and geotechnical sediment properties has been observed in previous field studies (Stark and Brilli, 2021), and numerical simulations show that local heterogeneity of hydraulic conductivity and capillarity can significantly affect soil moisture contents and groundwater dynamics on beaches (Geng et al., 2020).

In an area with such a large spatial variability of surface moisture, it is inherently difficult to obtain a good fit when comparing spatially and temporally averaged model results to point data. Despite large absolute errors in the model simulations, the mean error was only $-0.01 \text{ m}^3/\text{m}^3$. This result is promising, considering that the model parameters were not calibrated except for the hydraulic conductivity; the other values were derived from data or the literature. Furthermore, in mesoscale aeolian transport simulations, the small spatial offsets that resulted in large deviations between model results and observations are typically negligible. At decadal timescales, the high-resolution bathymetry that was

available for this study is typically not available, and local variability of porosity is not accounted for.

The sensitivity analysis indicated that the model is stable for a range of parameter settings, and most of the model inputs are commonly available data. However, estimation of the soil hydraulic properties can be resource-demanding and are typically not available for coastal engineering applications. To facilitate application of the model, sediment samples have been collected from ten beaches in Sweden and the Netherlands. Their drying and wetting soil water retention have been analysed using the same method outlined in this paper. The data is presented in Appendix C together with sieving protocols to facilitate model application at beaches with similar grain size distributions. All samples are duplicates to allow for an estimate of the uncertainty related to the analysis method and sediment heterogeneity.

When applying the proposed surface moisture model in AeoliS, it is important to select hydraulic properties that are representative of the local beach sand since they greatly influence surface moisture, specifically in the intertidal area (Schmutz, 2014). Finer-grained beaches typically have higher capillarity, lower hydraulic conductivity, and milder beach slopes, which all contribute to higher surface moisture content (Schmutz, 2014). At the same time, finer-grained beaches typically display larger potential transport rates due to lower threshold shear velocities for initiation of aeolian transport compared to coarser-grained beaches (Bagnold, 1941). Thus, when simulating aeolian transport rates on beaches, it is important to account for grain size effects on both transport rates and surface moisture contents.

Future studies should focus on validating the proposed surface moisture model with data sets displaying more variable meteorological conditions. Longer time series could be used to investigate the influence of surface moisture on yearly to decadal transport rates towards the dunes. However, further research is needed on how to include snow and frozen conditions (McKenna-Neuman and Nickling, 1989; Ollerhead et al., 2013; van Dijk and Law, 1995), as well as how the surface moisture influences the aeolian transport rates (Cornelis and Gabriels, 2003; Namikas and Sherman, 1995; Zambrano-Cruzatty et al., 2019).

7. Conclusions

In this study, a new surface moisture module was implemented in the aeolian transport model AeoliS. The model includes the relevant processes to describe surface moisture at sandy beaches from the water line to the dune toe: tide and wave-induced groundwater variations, wave runup, capillary rise, percolation, precipitation, and evaporation. The model was tested against a data set of 221 observations from three sampling occasions at Noordwijk beach in the Netherlands in January, March, and April 2020. The results were partly poor, where large deviations occurred between observed and simulated moisture contents (MAE = $0.07 \text{ m}^3/\text{m}^3$). The complexity of the intertidal area at the study site causes large local gradients in moisture content, meaning that a small spatial offset can result in a large error. Furthermore, the measured surface moisture data indicates that local variability of hydraulic properties can have a significant impact on the surface moisture. This variability was not accounted for within the model, which assumed uniform hydraulic properties. Still, with limited calibration, the model represented the average moisture conditions well (ME = $-0.01 \text{ m}^3/\text{m}^3$) and described the cross-shore moisture gradient. The proposed model provides a promising starting point to further explore surface moisture processes on sandy beaches and to include surface moisture in mesoscale aeolian transport simulations.

CRediT authorship contribution statement

Caroline Hallin: Conceptualization, Methodology, Formal analysis, Writing – original draft. **Christa van IJzendoorn:** Investigation, Writing – review & editing. **Jan-Markus Homberger:** Investigation, Writing – review & editing. **Sierd de Vries:** Supervision, Writing –

review & editing, Project administration, Funding acquisition.

Declaration of competing interest

The authors declare that they have no known competing financial interests or personal relationships that could have appeared to influence the work reported in this paper.

Data availability

Data will be made available on request.

Appendix A. Numerical solution of the Boussinesq equation

The Boussinesq equation is solved numerically with a central finite difference method in space and a fourth-order Runge-Kutta integration technique in time,

$$f(\eta) = \frac{K}{n_e} \left[\underbrace{D \frac{\partial^2 \eta}{\partial x^2}}_a + \underbrace{\frac{\partial}{\partial x} \left\{ \eta \frac{\partial \eta}{\partial x} \right\}}_b \right] \underbrace{\quad}_c$$

The Runge-Kutta time-stepping, where Δt is the length of the timestep, is defined as,

$$\eta_i^{t+1} = \eta_i^t + \frac{\Delta t}{6} (f_1 + 2f_2 + 2f_3 + f_4)$$

$$f_1 = f(\eta_i^t)$$

$$f_2 = f\left(\eta_i^t + \frac{\Delta t}{2} f_1\right)$$

$$f_3 = f\left(\eta_i^t + \frac{\Delta t}{2} f_2\right)$$

$$f_4 = f(\eta_i^t + \Delta t f_3)$$

where, i is the grid cell in x -direction and t is the timestep. The central difference solution to $f(\eta)$ is obtained through discretisation of the Boussinesq equation,

$$a_i = \frac{\eta_{i+1} - 2\eta_i + \eta_{i-1}}{(\Delta x)^2}$$

$$b_i = \frac{\eta_i(\eta_{i+1} - \eta_{i-1})}{\Delta x}$$

$$c_i = \frac{(b_{i+1} - b_{i-1})}{\Delta x}$$

Appendix B. Penman equation

The evaporation E (mm/day) is computed with the Penman equation following the method outlined in [Shuttleworth \(1993\)](#),

$$E = \frac{m_v R_n + 6.43 \gamma \delta_e (a_u + b_u u_2)}{\lambda (m_v + \gamma)}$$

where R_n is the net radiation (MJ/m²/d) (obtained directly from meteorological data: "global radiation"), λ is the latent heat of vaporisation (estimated to be about 2.26 MJ/kg), m_v is the gradient of the saturation vapour pressure (kPa/°C), γ is the psychrometric coefficient (kPa/°C), δ_e is vapour pressure deficit (kPa), u_2 is the wind speed at 2 m height (m/s) and a_u and b_u are coefficients. In the original Penman equation, $a_u = 1$ and $b_u = 0.54$. However, a value of $b_u = 0.86$ following [Doorenbos and Pruitt \(1975\)](#) has been found to give better results on beaches ([Zhu, 2007](#)) and is subsequently used here.

The vapour pressure deficit, δ_e , is computed as the difference between the saturated pressure, e_s and actual pressure, which is computed from the relative humidity, RH (%),

Acknowledgements

We would like to acknowledge Professor Magnus Persson at Lund University (Sweden) for fruitful discussions and advice about hydrological processes, Sander Vos at TU Delft (the Netherlands) for providing topographic data from the Scanex experiment, and Bas Huisman at Deltares (the Netherlands) for providing the wave data.

The late Professor Sjoerd E. A. T. M. van der Zee at Wageningen University (the Netherlands) made significant contributions to the development of the model and this paper. We are ever grateful for his help and inspiration.

This work was supported by the Dutch Research Council (NWO) the DuneForce project (number 17064).

$$\delta_e = e_s \left(1 - \frac{RH}{100} \right)$$

Following Shuttleworth (1993), the saturated vapour, e_s (kPa), is estimated by the Tetens equation,

$$e_s = 0.6108 \exp\left(\frac{17.27T}{T + 237.3}\right)$$

where T is the air temperature ($^{\circ}\text{C}$). The gradient of the saturation vapour pressure, $m_v = de_s/dT$ (kPa/ $^{\circ}\text{C}$), is computed through (Shuttleworth, 1993),

$$m_v = \frac{4098e_s}{(237.3 + T)^2}$$

According to Shuttleworth, the psychrometric coefficient (kPa/ $^{\circ}\text{C}$) is estimated as,

$$\gamma_p = \frac{c_p p}{\epsilon \lambda} \cdot 10^{-3} = 0.0016286 \frac{p}{\lambda}$$

where c_p is the specific heat of moist air ($=1.013 \text{ kJ/kg/}^{\circ}\text{C}$), p is the atmospheric pressure (kPa), ϵ is the ratio of molecular weight of water vapour to that of dry air ($=0.622$), and λ is the latent heat of vaporisation of water (MJ/kg).

Appendix C. Soil water retention data

The soil water retention and grain size distribution have been analysed for duplicate samples from ten beaches in Sweden and the Netherlands. The results are summarized in the following tables.

Table C
1 Description of sediment samples.

No	Location	Date	Lat	Long
1	Knäbäckshusen	2020-10-25	55.640455	14.277987
2	Knäbäckshusen	2020-10-25	55.640455	14.277987
3	Vik-Baskemölla	2020-10-25	55.609688	14.298151
4	Vik-Baskemölla	2020-10-25	55.609688	14.298151
5	Tobisvik	2020-10-25	55.570823	14.339082
6	Tobisvik	2020-10-25	55.570823	14.339082
7	Kyhl	2020-10-25	55.437513	14.239806
8	Kyhl	2020-10-25	55.437513	14.239806
9	Sandhammaren	2020-10-25	55.385173	14.198745
10	Sandhammaren	2020-10-25	55.385173	14.198745
11	Ystad Sandskog	2020-10-25	55.425476	13.851464
12	Ystad Sandskog	2020-10-25	55.425476	13.851464
13	Zandmotor (intertidal area)	2020-11-06	52.051010	4.1828037
14	Zandmotor (intertidal area)	2020-11-06	52.051010	4.1828037
15	Zandmotor (dry beach)	2020-11-06	52.0513113	4.1834702
16	Zandmotor (dry beach)	2020-11-06	52.0513113	4.1834702
17	Texel Hors	2020-11-07	52.9870096	4.7327457
18	Texel Hors	2020-11-07	52.9870096	4.7327457
19	Terschelling Midsland	2020-11-08	53.4104718	5.2906955
20	Terschelling Midsland	2020-11-08	53.4104718	5.2906955
21	Noordwijk (south)	2020-11-09	52.2420398	4.4242766
22	Noordwijk (south)	2020-11-09	52.2420398	4.4242766
23	Noordwijk (north)	2020-11-09	52.2423986	4.4245955
24	Noordwijk (north)	2020-11-09	52.2423986	4.4245955

2 Sieve protocols. Mask size in μm , weights in g.

No	>2000	2000–420	420–210	210–150	150–105	105–63	63–50	<50
1	0.06	6.71	127.04	4.24	0.13	0.01	0.00	0.00
2	0.00	6.19	126.70	4.73	0.10	0.00	0.00	0.00
3	0.00	133.63	0.09	0.25	0.04	0.04	0.00	0.00
4	0.02	134.65	0.13	0.07	0.01	0.00	0.00	0.00
5	1.14	131.40	0.00	0.00	0.00	0.00	0.00	0.00
6	2.40	124.60	0.00	0.00	0.00	0.00	0.00	0.00
7	0.08	0.22	39.85	86.70	4.23	0.06	0.00	0.00
8	0.00	0.32	40.66	77.63	4.48	0.05	0.00	0.00
9	0.00	0.73	107.87	27.12	0.80	0.04	0.00	0.00
10	0.00	0.76	109.25	18.89	0.53	0.03	0.00	0.00
11	0.00	0.66	66.52	44.96	3.35	0.26	0.01	0.00
12	0.00	0.40	66.62	49.85	3.84	0.21	0.00	0.00

(continued on next page)

(continued)

No	>2000	2000–420	420–210	210–150	150–105	105–63	63–50	<50
13	0.00	18.14	110.51	8.69	0.77	0.03	0.00	0.00
14	0.00	36.37	91.42	3.06	0.30	0.01	0.00	0.00
15	0.76	30.13	88.32	23.24	7.21	1.27	0.00	0.00
16	1.62	30.37	83.00	22.76	6.76	1.39	0.00	0.00
17	0.00	2.31	86.54	40.78	0.77	0.02	0.00	0.00
18	0.00	4.25	97.79	40.05	0.84	0.01	0.00	0.00
19	0.00	0.02	66.66	56.87	1.48	0.07	0.00	0.00
20	0.19	0.06	76.33	54.52	1.82	0.09	0.00	0.00
21	0.06	2.10	65.17	56.47	7.37	0.16	0.00	0.00
22	0.03	2.52	71.01	55.24	9.45	0.18	0.00	0.00
23	2.91	42.09	45.31	87.39	8.60	1.18	0.02	0.00
24	0.54	31.17	99.35	13.38	2.07	0.03	0.01	0.00

3 Wetting soil water retention. Suction in pF and moisture content in m^3/m^3 .

No	1.8	1.6	1.5	1.4	1.2	1	0.7	0.4	0
1	0.02	0.02	0.04	0.07	0.23	0.27	0.29	0.31	0.35
2	0.05	0.04	0.04	0.04	0.23	0.27	0.28	0.30	0.36
3	0.03	0.03	0.03	0.03	0.03	0.05	0.19	0.26	0.32
4	0.03	0.03	0.03	0.03	0.03	0.06	0.18	0.26	0.31
5	0.02	0.02	0.02	0.02	0.02	0.02	0.08	0.22	0.31
6	0.02	0.02	0.02	0.02	0.02	0.02	0.07	0.22	0.30
7	0.03	0.09	0.18	0.30	0.32	0.32	0.33	0.35	0.38
8	0.04	0.09	0.16	0.28	0.30	0.31	0.31	0.33	0.38
9	0.11	0.11	0.14	0.18	0.31	0.32	0.33	0.34	0.39
10	0.05	0.05	0.09	0.16	0.31	0.32	0.33	0.34	0.39
11	0.12	0.13	0.15	0.20	0.25	0.26	0.27	0.30	0.34
12	0.04	0.04	0.08	0.19	0.27	0.28	0.28	0.31	0.36
13	0.03	0.03	0.04	0.07	0.20	0.28	0.30	0.31	0.34
14	0.03	0.03	0.03	0.05	0.15	0.26	0.32	0.34	0.36
15	0.03	0.04	0.09	0.14	0.24	0.26	0.27	0.28	0.31
16	0.03	0.04	0.08	0.13	0.24	0.26	0.27	0.28	0.33
17	0.05	0.07	0.09	0.16	0.26	0.27	0.28	0.30	0.34
18	0.06	0.07	0.10	0.18	0.27	0.28	0.29	0.31	0.36
19	0.26	0.26	0.26	0.28	0.30	0.30	0.30	0.31	0.35
20	0.23	0.23	0.23	0.25	0.28	0.28	0.28	0.30	0.34
21	0.09	0.12	0.16	0.24	0.28	0.29	0.29	0.30	0.35
22	0.06	0.09	0.15	0.24	0.28	0.29	0.29	0.31	0.35
23	0.02	0.02	0.03	0.06	0.22	0.25	0.27	0.28	0.32
24	0.07	0.07	0.08	0.11	0.26	0.28	0.29	0.30	0.35

4 Drying soil water retention. Suction in pF and moisture content in m^3/m^3 .

No	0.4	0.7	1	1.2	1.4	1.5	1.6	1.8	2	3
1	0.34	0.34	0.31	0.30	0.24	0.12	0.06	0.04	0.03	0.02
2	0.36	0.34	0.29	0.29	0.25	0.12	0.06	0.06	0.05	0.02
3	0.30	0.29	0.11	0.05	0.03	0.03	0.03	0.03	0.03	0.02
4	0.29	0.29	0.11	0.04	0.03	0.03	0.03	0.03	0.03	0.03
5	0.29	0.21	0.03	0.03	0.03	0.03	0.03	0.03	0.02	0.02
6	0.29	0.22	0.03	0.03	0.02	0.02	0.02	0.02	0.02	0.03
7	0.37	0.37	0.36	0.36	0.36	0.36	0.35	0.05	0.04	0.02
8	0.37	0.36	0.34	0.34	0.34	0.34	0.33	0.08	0.04	0.02
9	0.38	0.37	0.37	0.37	0.36	0.30	0.19	0.16	0.14	0.02
10	0.38	0.37	0.36	0.36	0.35	0.30	0.14	0.05	0.05	0.02
11	0.33	0.31	0.29	0.29	0.28	0.28	0.20	0.14	0.13	0.02
12	0.35	0.34	0.31	0.31	0.31	0.30	0.20	0.04	0.04	0.02
13	0.33	0.32	0.28	0.27	0.17	0.09	0.05	0.03	0.03	0.01
14	0.35	0.34	0.27	0.24	0.11	0.07	0.04	0.03	0.03	0.01
15	0.30	0.29	0.26	0.26	0.23	0.16	0.10	0.05	0.03	0.01
16	0.32	0.31	0.27	0.26	0.22	0.15	0.10	0.04	0.03	0.01
17	0.33	0.32	0.30	0.30	0.30	0.28	0.20	0.06	0.05	0.02
18	0.35	0.34	0.32	0.32	0.32	0.31	0.22	0.06	0.06	0.02
19	0.33	0.32	0.31	0.31	0.31	0.31	0.29	0.26	0.26	0.02
20	0.34	0.31	0.30	0.30	0.30	0.29	0.25	0.23	0.23	0.03
21	0.33	0.33	0.33	0.33	0.32	0.32	0.29	0.13	0.11	0.02
22	0.34	0.34	0.33	0.33	0.32	0.32	0.28	0.06	0.06	0.02
23	0.31	0.30	0.30	0.29	0.26	0.12	0.04	0.02	0.02	0.01
24	0.33	0.32	0.33	0.33	0.32	0.20	0.09	0.06	0.07	0.01

References

- Baart, F., Bakker, M.A.J., Van Dongeren, A., Den Heijer, C., Van Heteren, S., Smit, M.W. J., Van Koningsveld, M., Pool, A., 2011. Using 18th century storm-surge data from the Dutch Coast to improve the confidence in flood-risk estimates. *Nat. Hazards Earth Syst. Sci.* 11, 2791–2801. <https://doi.org/10.5194/nhess-11-2791-2011>.
- Bagnold, R.A., 1941. *The Physics of Blown Sand and Desert Dunes*. Meuthen, London.
- Bagnold, R.A., 1937. The transport of sand by wind. *Geogr. J.* 89, 409–438.
- Baird, A.J., Mason, T., Horn, D.P., 1998. Validation of a Boussinesq model of beach ground water behaviour. *Mar. Geol.* 148, 55–69. [https://doi.org/10.1016/S0025-3227\(98\)00026-7](https://doi.org/10.1016/S0025-3227(98)00026-7).
- Barchyn, T.E., Martin, R., Kok, J., Hugenoltz, C.H., 2014. Fundamental mismatches between measurements and models in aeolian sediment transport prediction: the role of small-scale variability. *Aeolian Res* 15, 245–251. <https://doi.org/10.1016/j.aeolia.2014.07.002>.
- Bauer, B.O., Davidson-Arnott, R.G.D., Hesp, P., Namikas, S.L., Ollerhead, J., Walker, I.J., 2009. Aeolian sediment transport on a beach: surface moisture, wind fetch, and mean transport. *Geomorphology* 105, 106–116. <https://doi.org/10.1016/j.geomorph.2008.02.016>.
- Bilskie, M.V., Hagen, S.C., Medeiros, S.C., Passeri, D.L., 2014. Dynamics of Sea Level Rise and Coastal Flooding 927–934. <https://doi.org/10.1002/2013GL058759>. *Standard*.
- Booij, N., Ris, R.C., Holthuijsen, L.H., 1999. A third-generation wave model for coastal regions, Part I, Model description and validation. *J. Geophys. Res.* 104, 7649–7666.
- Boufadel, M.C., Suidan, M.T., Venosa, A.D., 1999. A numerical model for density-and-viscosity-dependent flows in two-dimensional variably saturated porous media. *J. Contam. Hydrol.* 37 [https://doi.org/10.1016/S0169-7722\(98\)00164-8](https://doi.org/10.1016/S0169-7722(98)00164-8).
- Brakenhoff, L.B., Smit, Y., Donker, J.J.A., Ruessink, G., 2019. Tide-induced variability in beach surface moisture: observations and modelling. *Earth Surf. Process. Landforms* 44, 317–330. <https://doi.org/10.1002/esp.4493>.
- Brand, E., Ramaekers, G., Lodder, Q., 2022. Dutch experience with sand nourishments for dynamic coastline conservation – an operational overview. *Ocean Coast Manag.* 217, 106008 <https://doi.org/10.1016/j.ocecoaman.2021.106008>.
- BS1377-2, 1990. Part 2: classification tests. In: *Methods of Tests for Soils for Civil Engineering Purposes*. British Standard, London.
- Chepil, W.S., 1956. Influence of soil moisture on erodibility of soil by wind. *Soil Sci. Soc. Am. Proc.* 20, 288–292.
- Cornelis, W.M., Gabriels, D., 2003. The effect of surface moisture on the entrainment of dune sand by wind: an evaluation of selected models. *Sedimentology* 50, 771–790. <https://doi.org/10.1046/j.1365-3091.2003.00577.x>.
- Davidson-Arnott, R.G., MacQuarrie, K., Aagaard, T., 2005. The effect of wind gusts, moisture content and fetch length on sand transport on a beach. *Geomorphology* 68, 115–129. <https://doi.org/10.1016/j.geomorph.2004.04.008>.
- de Groot, A.V., Veeneklaas, R.M., Bakker, J.P., 2011. Sand in the salt marsh: contribution of high-energy conditions to salt-marsh accretion. *Mar. Geol.* 282, 240–254. <https://doi.org/10.1016/j.margeo.2011.03.002>.
- de Vries, S., Southgate, H.N., Kanning, W., Ranasinghe, R., 2012. Dune behavior and aeolian transport on decadal timescales. *Coast. Eng.* 67, 41–53. <https://doi.org/10.1016/j.coastaleng.2012.04.002>.
- Delgado-Fernandez, I., 2010. A review of the application of the fetch effect to modelling sand supply to coastal foredunes. *Aeolian Res* 2, 61–70. <https://doi.org/10.1016/j.aeolia.2010.04.001>.
- Di Biase, V., Hanssen, R.F., Vos, S.E., 2021. Sensitivity of near-infrared permanent laser scanning intensity for retrieving soil moisture on a coastal beach: calibration procedure using in situ data. *Rem. Sens.* 13 <https://doi.org/10.3390/rs13091645>.
- Dirksen, C., 1999. *Soil Physics Measurements*. GeoEcology paperback.
- Doody, P., Ferreira, M., Lombardo, S., Lucius, I., Misdorp, R., Niesing, H., Salman, A., Smallegange, M., 2004. *Living with Coastal Erosion in Europe: Sediment and Space for Sustainability: Results from the EUROSION Study*. European Commission, Luxembourg.
- Doorenbos, J., Pruitt, W.O., 1975. *Crop water requirement*. Irrigat. Drain. 24 (Rome).
- Durán, O., Moore, L.J., 2013. Vegetation controls on the maximum size of coastal dunes. *Proc. Natl. Acad. Sci. U.S.A.* 110, 17217–17222. <https://doi.org/10.1073/pnas.1307580110>.
- Edwards, B.L., Schmutz, P.P., Namikas, S.L., 2013. Comparison of surface moisture measurements with depth-integrated moisture measurements on a fine-grained beach. *J. Coast Res.* 29, 1284. <https://doi.org/10.2112/jcoastres-d-12-00008.1>.
- Geng, X., Heiss, J.W., Michael, H.A., Boufadel, M.C., 2017. Subsurface flow and moisture dynamics in response to swash motions: effects of beach hydraulic conductivity and capillarity. *Water Resour. Res.* 53, 10317–10335. <https://doi.org/10.1002/2017WR021248>.
- Geng, X., Heiss, J.W., Michael, H.A., Boufadel, M.C., Lee, K., 2020. Groundwater flow and moisture dynamics in the swash zone: effects of heterogeneous hydraulic conductivity and capillarity. *Water Resour. Res.* 56, 1–21. <https://doi.org/10.1029/2020WR028401>.
- Groot, A. De, Berendse, F., Riksen, M., Baas, A., Slim, P., Dobben, H. Van, Stroosnijder, L., 2011. Modelling coastal dune formation and associated vegetation development. *Geophys. Res. Abstr.* 13, 4959.
- Hage, P., Ruessink, G., Aartrijk, Z. Van, Donker, J., 2020. Using video monitoring to test a fetch-based aeolian sand transport model. *J. Mar. Sci. Eng.* 8, 1–22. <https://doi.org/10.3390/jmse8020110>.
- Hanson, H., Larson, M., 2008. Implications of extreme waves and water levels in the southern Baltic Sea. *J. Hydraul. Res.* 46, 292–302. <https://doi.org/10.1080/00221686.2008.9521962>.
- Heiss, J.W., Puleo, J.A., Ullman, W.J., Michael, H.A., 2015. Coupled surface-subsurface hydrologic measurements reveal infiltration, recharge, and discharge dynamics across the swash zone of a sandy beach. *Water Resour. Res.* 51 <https://doi.org/10.1002/2015WR017395>.
- Heiss, J.W., Ullman, W.J., Michael, H.A., 2014. Swash zone moisture dynamics and unsaturated infiltration in two sandy beach aquifers. *Estuar. Coast Shelf Sci.* 143, 20–31. <https://doi.org/10.1016/j.ecss.2014.03.015>.
- Hoonhout, B., de Vries, S., 2019. Simulating spatiotemporal aeolian sediment supply at a mega nourishment. *Coast. Eng.* 145, 21–35. <https://doi.org/10.1016/j.coastaleng.2018.12.007>.
- Hoonhout, B., de Vries, S., Cohn, N., 2015. The Influence of Spatially Varying Supply on Coastal Aeolian Transport : a Field Experiment. *Coast. Sediments* 2015 1–11.
- Hoonhout, B.M., de Vries, S., 2016. A process-based model for aeolian sediment transport and spatiotemporal varying sediment availability. *J. Geophys. Res.* <https://doi.org/10.1002/2015JF003692>.
- Horn, D.P., 2006. Measurements and modelling of beach groundwater flow in the swash-zone: a review. *Contin. Shelf Res.* 26, 622–652. <https://doi.org/10.1016/j.csr.2006.02.001>.
- Horn, D.P., 2002. Beach groundwater dynamics. *Geomorphology* 48, 121–146. [https://doi.org/10.1016/S0169-555X\(02\)00178-2](https://doi.org/10.1016/S0169-555X(02)00178-2).
- Hsu, S.-A., 1971. Wind stress criteria in eolian sand transport. *J. Geophys. Res.* 76, 8684–8686.
- Kang, H.Y., Nielsen, P., Hanslow, D., 1994. Watertable overheight due to wave runup on a sandy beach. *Coast. Eng.* 2115–2124, 1994.
- Kawamura, R., 1951. Study on sand movement by wind. *Reports Phys. Sci. Res. Inst. Tokyo Univ.* 5 (3–4), 95–112.
- KNMI, 2022. *Uurgegevens van het weer in Nederland [WWW Document]*. URL <https://www.knmi.nl/nederland-nu/klimatologie/uurgegevens>. (Accessed 2 March 2022).
- Kriebel, D.L., Dean, R.G., 1985. Numerical simulation of time-dependent beach and dune erosion. *Coast. Eng.* 9, 221–245. [https://doi.org/10.1016/0378-3839\(85\)90009-2](https://doi.org/10.1016/0378-3839(85)90009-2).
- Larson, M., Kraus, N.C., 1989. *SBEACH: Numerical Model for Simulating Storm-Induced Beach Change, Report 1: Empirical Foundation and Model Development*. U.S. Army Eng. Waterw. Exp. Station. *Coast. Eng. Res. Center, Vicksburg, MS. Tech. Rep. CERC-89-9*.
- Lettau, K., Lettau, H., 1978. Experimental and micrometeorological field studies of dune migration. In: Lettau, H., Lettau, K. (Eds.), *Exploring the World's Driest Climate*. University of Wisconsin-Madison.
- Li, L., Barry, D.A., Pattiaratchi, C.B., Masselink, G., 2002. Beachwin: modelling groundwater effects on swash sediment transport and beach profile changes. *Environ. Model. Software* 17, 313–320. [https://doi.org/10.1016/S1364-8152\(01\)00066-4](https://doi.org/10.1016/S1364-8152(01)00066-4).
- Line, D.E., Harman, W.A., Jennings, G.D., Thompson, E.J., 2014. IPCC: climate change 2014: synthesis report. In: Pachauri, R.K., Meyer, L.A. (Eds.), *Contribution of Working Groups I, II and III to the Fifth Assessment Report of the Intergovernmental Panel on Climate Change*.
- Liu, P.L.F., Wen, J., 1997. Nonlinear diffusive surface waves in porous media. *J. Fluid Mech.* 347, 119–139. <https://doi.org/10.1017/S0022112097006472>.
- McCall, R.T., Masselink, G., Poate, T.G., Roelvink, J.A., Almeida, L.P., Davidson, M., Russell, P.E., 2014. Modelling storm hydrodynamics on gravel beaches with XBeach. *G. Coast. Eng.* 91, 231–250. <https://doi.org/10.1016/j.coastaleng.2014.06.007>.
- McKenna-Neuman, C., Nickling, W.G., 1989. A theoretical and wind tunnel investigation of the effect of capillary water on the entrainment of sediment. *Can. J. Soil Sci.* 69, 76–96.
- Mualem, Y., 1974. A conceptual model of hysteresis. *Water Resour. Res.* 10, 514–520.
- Namikas, S.L., Sherman, D.J., 1995. A review of the effects of surface moisture content on aeolian sand transport. *Desert Aeolian Process* 269–293. https://doi.org/10.1007/978-94-009-0067-7_13.
- Nickling, W.G., Mc Kenna Neumann, C., 1995. Development of deflation lag surfaces. *Sedimentology* 42, 403–414. <https://doi.org/10.1111/j.1365-3091.1995.tb00381.x>.
- Nielsen, P., 2009. *Coastal and Estuarine Processes*. World Scientific Publishing Company.
- Nielsen, P., 1990. Tidal dynamics of the water table in beaches. *Water Resour. Res.* 26, 2127–2134. <https://doi.org/10.1029/WR026i009p02127>.
- Nielsen, P., Davis, G., Winterbourne, J., Elias, G., 1988. *Wave Setup and the Watertable in Sandy Beaches*. New South Wales Public Works Department Coastal Branch. Technical Report Technical Memo- randum 88/1.
- Nishi, R., Kraus, N.C., 1996. Mechanism and calculation of sand dune erosion by storms. In: *Proceedings of the 25th Coastal Engineering Conference*. ASCE, pp. 3034–3047.
- Nolet, C., Poortinga, A., Roosjen, P., Bartholomeus, H., Ruessink, G., 2014. Measuring and modeling the effect of surface moisture on the spectral reflectance of coastal beach sand. *PLoS One* 9, 1–9. <https://doi.org/10.1371/journal.pone.0112151>.
- Nordstrom, K.F., 2000. *Beaches and Dunes on Developed Coasts*. Cambridge University Press, UK.
- Ojeda, E., Ruessink, B.G., Guillen, J., 2008. Morphodynamic response of a two-barred beach to a shoreface nourishment. *Coast. Eng.* 55, 1185–1196. <https://doi.org/10.1016/j.coastaleng.2008.05.006>.
- Ollerhead, J., Davidson-Arnott, R., Walker, I.J., Mathew, S., 2013. Annual to decadal morphodynamics of the foredune system at greenwich dunes, prince edward Island, Canada. *Earth Surf. Process. Landforms* 38, 284–298. <https://doi.org/10.1002/esp.3327>.
- Overton, M.F., Fisher, J.S., Young, M.A., 1988. Laboratory investigation of dune erosion. *J. Waterw. Port. Coast. Ocean Eng.* 114, 367–373. [https://doi.org/10.1061/\(ASCE\)0733-950X\(1988\)114:3\(367\)](https://doi.org/10.1061/(ASCE)0733-950X(1988)114:3(367)).
- Owen, P., 1964. Saltation of uniform grains in air. *J. Fluid Mech.* 20, 225–242.
- Paldor, A., Stark, N., Florence, M., Raubenheimer, B., Elgar, S., Housego, R., Frederiks, R. S., Michael, H.A., 2022. Coastal topography and hydrogeology control critical groundwater gradients and potential beach surface instability during storm surges. *Hydrol. Earth Syst. Sci.* 26, 5987–6002. <https://doi.org/10.5194/hess-26-5987-2022>.

- Paprocki, J., Stark, N., Graber, H.C., Wadman, H., McNinch, J.E., 2022. Assessment of moisture content in sandy beach environments from multispectral satellite imagery. *Can. Geotech. J.* 59, 225–238. <https://doi.org/10.1139/cgj-2020-0624>.
- Paprocki, J., Stark, N., McNinch, J.E., Wadman, H., 2019. Spatial and temporal variations in moisture content at a sandy beach and the impact on sediment strength. *GeoCongress* 258–265. <https://doi.org/10.1061/9780784482131.027>, 2019.
- Pham, H.Q., Fredlund, D.G., Barbour, S.L., 2005. A study of hysteresis models for soil-water characteristic curves. *Can. Geotech. J.* 42, 1548–1568. <https://doi.org/10.1139/t05-071>.
- Raubenheimer, B., Guza, R.T., Elgar, S., 1999. Tidal water table fluctuations in a sandy ocean beach. *Water Resour. Res.* 35, 2313–2320. <https://doi.org/10.1029/1999WR900105>.
- Rijkswaterstaat, 2022. Waterinfo [WWW Document]. URL <https://waterinfo.rws.nl/>. (Accessed 2 February 2022).
- Rijkswaterstaat, 2020. Jarkus grids [WWW Document]. URL https://opendap.deltares.nl/thredds/dodsC/opendap/rijkswaterstaat/jarkus/grids/jarkusKB119_3534.nc.html.
- Roelvink, D., Costas, S., 2019. Coupling nearshore and aeolian processes: XBeach and duna process-based models. *Environ. Model. Software* 115, 98–112. <https://doi.org/10.1016/j.envsoft.2019.02.010>.
- Roelvink, D., Reniers, A., van Dongeren, A., van Thiel de Vries, J., McCall, R., Lescinski, J., 2009. Modelling storm impacts on beaches, dunes and barrier islands. *Coast. Eng.* 56, 1133–1152. <https://doi.org/10.1016/j.coastaleng.2009.08.006>.
- Ruessink, G., Sterk, G., Smit, Y., De Winter, W., Hage, P., Donker, J.J.A., Arens, S.M., 2022. Predicting monthly to multi-annual foredune growth at a narrow beach. *Earth Surf. Process. Landforms* 47. <https://doi.org/10.1002/esp.5350>.
- Sauermann, G., Kroy, K., Herrmann, H.J., 2001. Continuum saltation model for sand dunes. *Phys. Rev. E: Stat., Nonlinear, Soft Matter Phys.* 64, 031305 <https://doi.org/10.1103/PhysRevE.64.031305>.
- Schmutz, P.P., 2014. Investigation of Factors Controlling the Dynamics of Beach Surface Moisture.
- Sherman, D.J., Bauer, O., 1993. Dynamics of beach-dune systems. *Prog. Phys. Geogr.* 17, 413–447.
- Shuttleworth, W.J., 1993. Evaporation. In: Maidment, D.R. (Ed.), *Handbook of Hydrology*. McGraw-Hill, New York, 4.1–4.53.
- Silva, F.G., Wijnberg, K., Groot, A.V. De, Hulscher, S., 2017. ON the importance of tidal inlet processes for coastal dune. *Coastal Dynamics* 1131–1141, 2017.
- Šimunek, J., Šejna, M., van Genuchten, M.T., 1998. The HYDRUS-1D Software Package for Simulating the One-Dimensional Movement of Water, Heat, and Multiple Solutes in Variably-Saturated Media.
- Smit, Y., Donker, J.J.A., Ruessink, G., 2019. Spatiotemporal surface moisture variations on a barred beach and their relationship with groundwater fluctuations. *Hydrology* 6. <https://doi.org/10.3390/hydrology6010008>.
- Smit, Y., Ruessink, G., Brakenhoff, L.B., Donker, J.J.A., 2018. Measuring spatial and temporal variation in surface moisture on a coastal beach with a near-infrared terrestrial laser scanner. *Aeolian Res* 31, 19–27. <https://doi.org/10.1016/j.aeolia.2017.07.004>.
- Stark, N., Brilli, N., 2021. Geotechnical investigation of spatiotemporal variations at a sand beach characterized by active erosion and sediment remobilization processes. In: 10th International Conference on Scour and Erosion (ICSE-10), pp. 1–10.
- Steezel, H.J., 1993. Cross-shore Transport during Storm Surges.
- Stive, M.J.F., Roelvink, D., J. A., de Vriend, H.J., 1990. Large-scale coastal evolution concept. In: *Coastal Engineering 1990*, pp. 1962–1974. <https://doi.org/10.1061/9780872627765.150>.
- Stockdon, H.F., Holman, R.A., Howd, P.A., Sallenger, A.H., 2006. Empirical parameterization of setup, swash, and runup. *Coast. Eng.* <https://doi.org/10.1016/j.coastaleng.2005.12.005>.
- Therrien, R., McLaren, R.G.G., Sudicky, E.A.A., Panday, S.M.M., 2010. HydroGeoSphere: a Three-Dimensional Numerical Model Describing Fully-Integrated Subsurface and Surface Flow and Solute Transport. Univ. Waterloo, Waterloo. Groundw. Simulations Group.
- Luna, M.C.M. de M., Parteli, E.J.R., Durán, O., Herrmann, H.J., 2011. Model for the genesis of coastal dune fields with vegetation. *Geomorphology* 129, 215–224. <https://doi.org/10.1016/j.geomorph.2011.01.024>.
- TNO, n.d. DINOloket Data en Informatie van de Nederlandse Ondergrond [WWW Document]. URL [DINOloket Data en Informatie van de Nederlandse Ondergrond](https://www.dinoloket.nl/) (accessed 2.3.22).
- Tuller, M., Or, D., 2005. Water retention and characteristic curve. In: Hillel, D. (Ed.), *Encyclopedia of Soils in the Environment*. Elsevier, Oxford, UK, pp. 278–289. <https://doi.org/10.1016/B0-12-348530-4/00376-3>.
- Turner, I.L., Nielsen, P., 1997. Rapid water table fluctuations within the beach face: Implications for swash zone sediment mobility? *Coast. Eng.* 32, 45–59. [https://doi.org/10.1016/S0378-3839\(97\)00015-X](https://doi.org/10.1016/S0378-3839(97)00015-X).
- Uphues, C.F.K., van IJendoorn, C.O., Hallin, C., Pearson, S.G., van Prooijen, B.C., Miot da Silva, G., de Vries, S., 2022. Coastal aeolian sediment transport in an active bed surface layer: tracer study and conceptual model. *Earth Surf. Process. Landforms* 47, 3147–3162. <https://doi.org/10.1002/esp.5449>.
- van der Werff, H.M.A., 2019. Mapping shoreline indicators on a sandy beach with supervised edge detection of soil moisture differences. *Int. J. Appl. Earth Obs. Geoinf.* 74, 231–238. <https://doi.org/10.1016/j.jag.2018.09.007>.
- van Dijk, D., Law, J., 1995. Sublimation and aeolian sand movement from a frozen surface: experimental results from Presqu'île beach, Ontario. *Geomorphology* 11, 177–187. [https://doi.org/10.1016/0169-555X\(94\)00065-Y](https://doi.org/10.1016/0169-555X(94)00065-Y).
- van Dijk, P.M., Arens, S.M., van Boxel, J.H., 1999. Aeolian processes across transverse dunes. II: modelling the sediment transport and profile development. *Earth Surf. Process. Landforms* 24, 319–333.
- van IJendoorn, C.O., de Vries, S., Hallin, C., Hesp, P.A., 2021. Sea level rise outpaced by vertical dune toe translation on prograding coasts. *Sci. Rep.* 11, 1–8. <https://doi.org/10.1038/s41598-021-92150-x>.
- van IJendoorn, C.O., Hallin, C., Cohn, N., Reniers, A.J.H.M., de Vries, S., 2022. Novel sediment sampling method provides new insights into vertical grain size variability due to marine and aeolian beach processes. *EarthSurface Process. Landforms* 1–19.
- van Rijn, L.C., Strypsteen, G., 2020. A fully predictive model for aeolian sand transport. *Coast. Eng.* 156 <https://doi.org/10.1016/j.coastaleng.2019.103600>.
- Vellinga, P., 1986. Beach and Dune Erosion during Storm Surges, 372. Dr. Thesis, Delft Univ. Technol. Delft, Netherlands Publ. [https://doi.org/10.1016/0378-3839\(82\)90007-2](https://doi.org/10.1016/0378-3839(82)90007-2). Delft Hydraul.
- Vos, S., Lindenberg, R., de Vries, S., 2017. CoastScan: continuous monitoring of coastal change using terrestrial laser scanning. *Coast. Dyn.* 2, 1518–1528.
- Wiggs, G.F.S., Baird, A.J., Atherton, R.J., 2004. The dynamic effects of moisture on the entrainment and transport of sand by wind. *Geomorphology* 59, 13–30. <https://doi.org/10.1016/j.geomorph.2003.09.002>.
- Wijnberg, K.M., 2002. Environmental controls on decadal morphologic behaviour of the Holland coast. *Mar. Geol.* 189, 227–247.
- Wijnberg, K.M., Terwindt, J.H.J., 1995. Extracting decadal morphological behaviour from high-resolution, long-term bathymetric surveys along the Holland coast using eigenfunction analysis 126, 301–330.
- Wong, P.P., Losada, I.J., Gattuso, J.P., Hinkel, J., Khattabi, A., McInnes, K.L., Saito, Y., Sallenger, A., Nicholls, R.J., Santos, F., Amezcua, S., 2015. Coastal systems and low-lying areas. In: *Climate Change 2014 Impacts, Adaptation and Vulnerability: Part A: Global and Sectoral Aspects*. <https://doi.org/10.1017/CBO9781107415379.010>.
- Zambrano-Cruzatty, L., Yerro, A., Stark, N., 2019. Influence of shear strength and moisture content on aeolian sand erosion. *GeoCongress* 1–10. <https://doi.org/10.1061/9780784482155.001>, 2019.
- Zhang, W., Schneider, R., Kolb, J., Teichmann, T., Dudzinska-nowak, J., Harff, J., Hanebuth, T.J.J., 2015a. Land – sea interaction and morphogenesis of coastal foredunes — a modeling case study from the southern Baltic Sea coast. *Coast. Eng.* 99, 148–166. <https://doi.org/10.1016/j.coastaleng.2015.03.005>.
- Zhang, W., Schneider, R., Kolb, J., Teichmann, T., Dudzinska-Nowak, J., Harff, J., Hanebuth, T.J.J., 2015b. Land-sea interaction and morphogenesis of coastal foredunes - a modeling case study from the southern Baltic Sea coast. *Coast. Eng.* 99 <https://doi.org/10.1016/j.coastaleng.2015.03.005>.
- Zhu, Y., 2007. Modeling Spatial and Temporal Variations of Surface Moisture Content and Groundwater Table Fluctuations on a Fine-Grained Beach. Padre Island, Texas.
- Zingg, A., 1953. Wind tunnel studies of the movement of sedimentary material. *Proc. 5th Hydraul. Conf. Bull.* 34, 111–135.